A probabilistic approach for the detection of bolt loosening in periodically supported structures endowed with bolted flange joints

Tao Yin [1*], Xiang-Yu Wang [2], Hong-Ping Zhu [3]

1. School of Civil Engineering, Wuhan University, Wuhan, 430072, P.R. China

2. Tandon School of Engineering, New York University, Brooklyn, NY 11201, U.S.A

3. School of Civil Engineering & Mechanics, Huazhong University of Science and Technology, Wuhan 430074, P.R. China

Abstract: From the literature, only very limited research activities have been carried out for fault diagnose of periodic structural system following model-based approaches. This paper focuses on the development of a practical methodology for modeling and detecting bolt loosening on periodically supported beam-type structure endowed with bolted flange joints, representing typical supported pipeline system in industry, through using measured modal parameters. Within the framework of periodic system, an efficient analytical model of the complete periodic system is first developed for dynamic analysis in frequency domain. The highly accurate spectral element method is employed to formulate the supercell-based dynamic stiffness matrix (DSM) of periodic cell containing bolted flange connection in the midspan, and the transfer matrix-based method is also developed for assembling the system DSM of entire periodic structural system through the obtained DSM of each individual cell, where the computational effort required in dynamic analysis of the complete periodic system with a large amount of repeated cells is almost comparable to a single cell. Then, in the proposed methodology, the statistical detection of bolt loosening is accomplished through two phases. The most plausible model class with appropriate parameterization complexity is first recognized by following the Bayesian model class selection strategy in the first phase. In the subsequent phase, the posterior probability density function of the stiffness scaling parameters is identified following the particle filter-based approach. To demonstrate and validate the proposed methodology, this paper reports not only the theoretical development but also a comprehensive series of numerical and experimental case studies, and corresponding results achieved are very encouraging.

Keywords: Periodic structure; bolt loosening detection; spectral element method; transfer matrix method; model class selection; particle filter.

[*] Corresponding author: Dr. Tao YIN, Associate Professor, School of Civil Engineering, Wuhan University, Wuhan, 430072, P. R. China. E-mail: tyin@whu.edu.cn

1. INTRODUCTION

The periodic structural system consists of amount of repeated units, which are joined together in an identical manner to form the whole structure. Periodic structures, such as phononic crystal [1], multi-span bridges, elevated guideways, pipeline, and rail-sleeper system, etc., have obtained extensive applications from solid-state physics [2] to various engineering industries [3-7]. It has been revealed that periodic structures possess a variety of interesting dynamical behaviors including the signature vibration band-gap phenomenon, i.e., they behave as mechanical band-pass filters, responding and radiating noise very efficiently in certain frequency bands while not so efficiently in other bands. Most of research activities related to periodic structures to date concentrate on structural vibration control and optimization design by employing the unique dynamical characteristics of periodic structures [8-14].

However, there exist no perfectly identical periodic elements due to manufacturing errors and damages in reality, and the presence of small irregularities or disorder may lead to the vibration localization [8], which might significantly affect dynamic characteristics of the periodic structures; however, the particular attention with respect to structural system identification and health monitoring [15,16] for this special type of structures by employing the inherent periodic property is seldom emphasized [17-19]. Investigation of the dynamical behavior of periodic structural system is thus very important for assessing the integrity of the entire structural system within the framework of vibration-based structural health monitoring [20-28].

A periodic structure of articulated beams with couplers, which consists of identical and uniform beams of finite length connected to adjoining ones by couplers at junctions, is one of the simplest models for pipelines [29,30]. Bolted-flange connection is one of the most commonly used coupler types in the pipeline industry. However, due to discontinuity of the structure, and mechanical contact and friction of the connecting interface, the connection becomes the major source of nonlinearity and uncertainty for the assembled structure [31], especially under dynamic loads [32]. Therefore, it’s very important to properly model the bolt-jointed connection for understanding the dynamic behaviors and accomplish the purpose of model-based bolt-loosening detection.

In the last almost five decades, the FE method has become the prevalent technique used for analyzing physical phenomena in various fields of research [33-38], and there are a large number of studies available in the literature applied for analyzing the mechanical fasteners from the theoretical as well as practical points of view following the FE method [39-41]. These modeling approaches can be mainly divided into two categories [42], i.e., node-to-node contact element and interface element methods. Among them, node-to-node contact element techniques

offer the possibility to implement various different types of friction and contact models, even a full 3D contact analysis. However, the main drawback lies in that the numerical effort increases drastically along with the increase of number of contact pairs contained in the structure, resulting in a decrease of efficiency and numerical stability. On the other hand, the interface element methods, generally referring to the thin-layer element and zero-thickness element theories [43-45], are initially developed in geomechanics [46] and later adopted in other engineering fields including the joint modeling. Both of them are parametric models and can be implemented relatively easy with existing FE software by using experimentally obtained joint parameters for dynamic analysis of assembled structural system. Nevertheless, it should be emphasized that the dominant limiting factor in these joint modeling techniques and similar others to date by FE approach for time- and frequency-domain analysis might still be the long simulation times [42], especially for the structure having a large number of joints. Furthermore, since the mass distribution of the conventional FE method is only approximate due to the static shape function adopted, the mesh density is forced to be fine enough especially for dynamic analysis, not to mention the nonlinear properties of bolted joint, if considered. Therefore, as for the periodically supported pipeline system with a large number of repeated units and bolted-joint connections investigated in the present paper, the analysis of dynamic response for such a large-scale assembled periodic structural system by the above-mentioned joint modeling strategies with the FE approach would be extremely difficult, if not impossible, due to the tremendous computational effort involved, which is also detrimental for model-based methods for the detection of bolt loosening.

Instead of using the conventional FE method, by employing the spectral element (SE) approach [47,48], this paper develops an analytical model of the periodically supported pipeline system with special attention paid to the bolted-flange joints for the purpose of linear dynamic analysis of the entire periodic system. Following the framework of periodic system, the structural component between two adjacent supports is treated as the periodic cell, which is split into a certain number of sub-cells regarding to the geometric configuration of bolted connection, and the preload effect of bolts is quantified by variable elastic modulus of a particular thin-layered sub-cell. By gathering all sub-cells following the SE procedure, the original cell with bolted flange joint is condensed into a two-node super-cell, from which the analytical model of the complete periodic pipeline system is developed. Moreover, by employing the transfer matrix theorem, the computational cost required in linear dynamic analysis of the complete periodic structural system can be dramatically reduced regardless of the number of contained periodic units, which is extremely appealing for periodic system with a huge number of repeated components.

In addition, based on the SE model developed for the periodically supported beam-type structure endowed with bolted flange connections, a statistical methodology is put forward subsequently for efficiently detecting loosening of bolted joint on this type of structural system utilizing measured modal parameters. The proposed detection methodology consists of two successive phases. In the first phase, different classes of models are proposed to model the periodic structural system with different parameterization schemes, and the Bayesian model class selection method is employed to identify the most plausible class of models with suitable parameterization complexity based on the measured modal parameters. In the subsequent phase, the posterior probability density function (PDF) is calculated following the particle filter-based approach to explicitly handle the uncertainties of the identified results due to various kinds of sources including measurement noise and modelling error. Thus, the proposed methodology not only identifies the scaling parameters to quantify the connection status of bolted flange joints with appropriate complexity of model class but also estimates the confidence level of the identified results, which are essential to make judgements on repair and maintenance work in real applications.

2. THEORETICAL DEVELOPMENT

2.1 Dynamic modeling of periodic system endowed with bolted flange joints

The schematic diagram of investigated periodically supported beam endowed with bolted-flange joints is shown in Fig. 1 by regarding the span with adjacent supports as the periodic cell. Fig. 2 shows the schematic diagram of the periodic cell containing bolted flange joints and its discretization strategy for implementing the spectral element method. Referring to this figure, the height of beam and bolted flange are H_B and H_F, while the span of periodic cell between two adjacent supports and the flange thickness are denoted by L and T_F, respectively. The thin-layer elements with height H_L and thickness T_L located between two flanges are proposed to simulate the bolted-flange connection. Fig. 3 provides the corresponding discretization model of a single cell, which is divided into ten sub-cells. The cross-section of two sub-cells 3 and 4 is assumed to be maintained with rigid plain, and the effect of stress singularity is also neglected for simplicity in the present paper.

Following the plane-section hypothesis and compatibility condition of displacement for sub-cells 1, 3, 5 and 8 as shown in Fig. 3, the displacement vector at nodes 7, 8 and 9 with respect to node 5 can be expressed as, respectively,

$$\mathbf{U}_{7,n} = \begin{Bmatrix} u_{7,n} \\ w_{7,n} \\ \phi_{7,n} \end{Bmatrix} = \begin{Bmatrix} u_{5,n} + h_1\phi_{5,n} \\ w_{5,n} \\ \phi_{5,n} \end{Bmatrix} = \mathbf{Q}_1\mathbf{U}_{5,n} \tag{1}$$

$$\mathbf{U}_{8,n} = \begin{Bmatrix} u_{8,n} \\ w_{8,n} \\ \phi_{8,n} \end{Bmatrix} = \begin{Bmatrix} u_{5,n} \\ w_{5,n} \\ \phi_{5,n} \end{Bmatrix} = \mathbf{U}_{5,n} \tag{2}$$

$$\mathbf{U}_{9,n} = \begin{Bmatrix} u_{9,n} \\ w_{9,n} \\ \phi_{9,n} \end{Bmatrix} = \begin{Bmatrix} u_{5,n} + h_2\phi_{5,n} \\ w_{5,n} \\ \phi_{5,n} \end{Bmatrix} = \mathbf{Q}_2\mathbf{U}_{5,n} \tag{3}$$

where, $\mathbf{U}_{i,n} = \{u_i \ w_i \ \phi_i\}^{\mathrm{T}}$, $i = 1,2,\ldots,20$ is the displacement vector at the node i, and $u_{i,n}$, $w_{i,n}$ and $\phi_{i,n}$ are displacement components corresponding to longitudinal, transversal and rotational directions, respectively. The subscript n denotes the related quantities which are evaluated at frequency ω_n in frequency-domain. $\mathbf{Q}_1$ and $\mathbf{Q}_2$ are both the transformation matrices between two displacement vectors and given by

$$\mathbf{Q}_1 = \begin{bmatrix} 1 & 0 & h_1 \\ 0 & 1 & 0 \\ 0 & 0 & 1 \end{bmatrix}, \quad \mathbf{Q}_2 = \begin{bmatrix} 1 & 0 & h_2 \\ 0 & 1 & 0 \\ 0 & 0 & 1 \end{bmatrix} \tag{4}$$

where, h_1 and h_2 are the transverse distances between neutral axis of sub-cell 1 and that of sub-cells 5 and 8, respectively.

The equilibrium equations of nodes 5, 7, 8 and 9 can be expressed as

$$\begin{Bmatrix} N_{5,n} \\ V_{5,n} \\ M_{5,n} \end{Bmatrix} + \begin{Bmatrix} N_{7,n} \\ V_{7,n} \\ M_{7,n} + h_1N_{7,n} \end{Bmatrix} + \begin{Bmatrix} N_{8,n} \\ V_{8,n} \\ M_{8,n} \end{Bmatrix} + \begin{Bmatrix} N_{9,n} \\ V_{9,n} \\ M_{9,n} + h_2N_{9,n} \end{Bmatrix} = \begin{Bmatrix} 0 \\ 0 \\ 0 \end{Bmatrix} \tag{5}$$

or, in matrix form as

$$\mathbf{F}_{5,n} + \mathbf{Q}_1{}^{\mathrm{T}}\mathbf{F}_{7,n} + \mathbf{F}_{8,n} + \mathbf{Q}_2{}^{\mathrm{T}}\mathbf{F}_{9,n} = \mathbf{0} \tag{6}$$

where $\mathbf{F}_{i,n} = \{N_{i,n} \ V_{i,n} \ M_{i,n}\}^{\mathrm{T}}$ are defined as the force vectors associated with node i, and $N_{i,n}$, $V_{i,n}$ and $M_{i,n}$ represent axial force, shear force and bending moment, respectively.

Similarly, the displacements at nodes 10, 11 and 12 can be represented by those of node 6, respectively, as

$$\mathbf{U}_{10,n} = \mathbf{Q}_1\mathbf{U}_{6,n}, \ \mathbf{U}_{11,n} = \mathbf{U}_{6,n}, \ \mathbf{U}_{12,n} = \mathbf{Q}_2\mathbf{U}_{6,n} \tag{7}$$

and the corresponding equilibrium equations of these nodes are given by

$$\mathbf{F}_{6,n} + \mathbf{Q}_1{}^{\mathrm{T}}\mathbf{F}_{10,n} + \mathbf{F}_{11,n} + \mathbf{Q}_2{}^{\mathrm{T}}\mathbf{F}_{12,n} = \mathbf{0} \tag{8}$$

It's further assumed that the contact effect between the opposite surfaces of two flanges is ignored, thus,

$$\mathbf{F}_{3,n} = \mathbf{0}, \ \ \mathbf{F}_{4,n} = \mathbf{0} \tag{9}$$

In general, the dynamic equilibrium equation for the eth sub-cell can be written by

$$\mathbf{D}_n^{(e)} \begin{Bmatrix} \mathbf{U}_{e_1,n} \\ \mathbf{U}_{e_2,n} \end{Bmatrix} = \begin{bmatrix} \mathbf{D}_{LL,n}^{(e)} & \mathbf{D}_{LR,n}^{(e)} \\ \mathbf{D}_{RL,n}^{(e)} & \mathbf{D}_{RR,n}^{(e)} \end{bmatrix} \begin{Bmatrix} \mathbf{U}_{e_1,n} \\ \mathbf{U}_{e_2,n} \end{Bmatrix} = \begin{Bmatrix} \mathbf{F}_{e_1,n} \\ \mathbf{F}_{e_2,n} \end{Bmatrix} \tag{10}$$

where, $\mathbf{D}_{LL,n}^{(e)}$, $\mathbf{D}_{LR,n}^{(e)}$, $\mathbf{D}_{RL,n}^{(e)}$ and $\mathbf{D}_{RR,n}^{(e)} \in \mathbb{R}^{3\times3}$ are the partitioned matrices of DSM $\mathbf{D}_n^{(e)} \in \mathbb{R}^{6\times6}$ for the eth sub-cell, and $e = 1,2,\dots,10$ represent the sub-cell numbers as shown in Fig. 3. The DSM with sub-cell numbers ranging from 1 to 10 except for 6 and 9 is provided in the Appendix A, and the remaining two are given in the Appendix B. The subscript pairs $\{e_1, e_2\}$ denote the node numbers associated with left and right ends of the eth sub-cell.

Specifically, referring to Fig. 3, the equilibrium equations for sub-cells 1 and 2 can be provided, respectively, as

$$\begin{bmatrix} \mathbf{D}_{LL,n}^{(1)} & \mathbf{D}_{LR,n}^{(1)} \\ \mathbf{D}_{RL,n}^{(1)} & \mathbf{D}_{RR,n}^{(1)} \end{bmatrix} \begin{Bmatrix} \mathbf{U}_{1,n} \\ \mathbf{U}_{5,n} \end{Bmatrix} = \begin{Bmatrix} \mathbf{F}_{1,n} \\ \mathbf{F}_{5,n} \end{Bmatrix} \tag{11}$$

$$\begin{bmatrix} \mathbf{D}_{LL,n}^{(2)} & \mathbf{D}_{LR,n}^{(2)} \\ \mathbf{D}_{RL,n}^{(2)} & \mathbf{D}_{RR,n}^{(2)} \end{bmatrix} \begin{Bmatrix} \mathbf{U}_{6,n} \\ \mathbf{U}_{2,n} \end{Bmatrix} = \begin{Bmatrix} \mathbf{F}_{6,n} \\ \mathbf{F}_{2,n} \end{Bmatrix} \tag{12}$$

By utilizing Eqs. (2), (4) and (7) to represent $\mathbf{U}_{8,n}$ and $\mathbf{U}_{11,n}$ in terms of $\mathbf{U}_{5,n}$ and $\mathbf{U}_{6,n}$, respectively, the equilibrium equations for sub-cells 3 and 4 can be further given by

$$\begin{bmatrix} \mathbf{D}_{LL,n}^{(3)} & \mathbf{D}_{LR,n}^{(3)} \\ \mathbf{D}_{RL,n}^{(3)} & \mathbf{D}_{RR,n}^{(3)} \end{bmatrix} \begin{Bmatrix} \mathbf{U}_{8,n} \\ \mathbf{U}_{3,n} \end{Bmatrix} = \begin{bmatrix} \mathbf{D}_{LL,n}^{(3)} & \mathbf{D}_{LR,n}^{(3)} \\ \mathbf{D}_{RL,n}^{(3)} & \mathbf{D}_{RR,n}^{(3)} \end{bmatrix} \begin{Bmatrix} \mathbf{U}_{5,n} \\ \mathbf{U}_{3,n} \end{Bmatrix} = \begin{Bmatrix} \mathbf{F}_{8,n} \\ \mathbf{F}_{3,n} \end{Bmatrix} \tag{13}$$

$$\begin{bmatrix} \mathbf{D}_{LL,n}^{(4)} & \mathbf{D}_{LR,n}^{(4)} \\ \mathbf{D}_{RL,n}^{(4)} & \mathbf{D}_{RR,n}^{(4)} \end{bmatrix} \begin{Bmatrix} \mathbf{U}_{4,n} \\ \mathbf{U}_{11,n} \end{Bmatrix} = \begin{bmatrix} \mathbf{D}_{LL,n}^{(4)} & \mathbf{D}_{LR,n}^{(4)} \\ \mathbf{D}_{RL,n}^{(4)} & \mathbf{D}_{RR,n}^{(4)} \end{bmatrix} \begin{Bmatrix} \mathbf{U}_{4,n} \\ \mathbf{U}_{6,n} \end{Bmatrix} = \begin{Bmatrix} \mathbf{F}_{4,n} \\ \mathbf{F}_{11,n} \end{Bmatrix} \tag{14}$$

The displacements and corresponding equilibrium equations at nodes 13, 14, 15 and 16 can be expressed as,

$$\mathbf{U}_{13,n} = \mathbf{U}_{14,n}, \ \ \mathbf{U}_{15,n} = \mathbf{U}_{16,n}, \ \ \mathbf{F}_{13,n} + \mathbf{F}_{14,n} = \mathbf{0}, \ \ \mathbf{F}_{15,n} + \mathbf{F}_{16,n} = \mathbf{0} \tag{15}$$

And the equilibrium equations for sub-cells 5 and 7 are given as,

$$\begin{bmatrix} \mathbf{D}_{LL,n}^{(5)} & \mathbf{D}_{LR,n}^{(5)} \\ \mathbf{D}_{RL,n}^{(5)} & \mathbf{D}_{RR,n}^{(5)} \end{bmatrix} \begin{Bmatrix} \mathbf{U}_{7,n} \\ \mathbf{U}_{13,n} \end{Bmatrix} = \begin{Bmatrix} \mathbf{F}_{7,n} \\ \mathbf{F}_{13,n} \end{Bmatrix} \tag{16}$$

$$\begin{bmatrix} \mathbf{D}_{LL,n}^{(7)} & \mathbf{D}_{LR,n}^{(7)} \\ \mathbf{D}_{RL,n}^{(7)} & \mathbf{D}_{RR,n}^{(7)} \end{bmatrix} \begin{Bmatrix} \mathbf{U}_{16,n} \\ \mathbf{U}_{10,n} \end{Bmatrix} = \begin{Bmatrix} \mathbf{F}_{16,n} \\ \mathbf{F}_{10,n} \end{Bmatrix} \tag{17}$$

By employing Eqs. (15) to (17) together with the dynamic equilibrium equations of sub-cell 6 provided in the Appendix B (see Eq. (B14)), the assembled dynamic equilibrium equations of sub-cells 5, 6 and 7 is given by

$$\begin{bmatrix} \mathbf{D}_{LL,n}^{(5)} & \mathbf{D}_{LR,n}^{(5)} & \mathbf{0} & \\ \mathbf{D}_{RL,n}^{(5)} & \mathbf{D}_{RR,n}^{(5)} + \mathbf{D}_{LL,n}^{(6)} & \mathbf{D}_{LR,n}^{(6)} & \\ & \mathbf{D}_{RL,n}^{(6)} & \mathbf{D}_{RR,n}^{(6)} + \mathbf{D}_{LL,n}^{(7)} & \mathbf{D}_{LR,n}^{(7)} \\ \mathbf{0} & & \mathbf{D}_{RL,n}^{(7)} & \mathbf{D}_{RR,n}^{(7)} \end{bmatrix} \begin{Bmatrix} \mathbf{U}_{7,n} \\ \mathbf{U}_{13,n} \\ \mathbf{U}_{16,n} \\ \mathbf{U}_{10,n} \end{Bmatrix} = \begin{Bmatrix} \mathbf{F}_{7,n} \\ \mathbf{0} \\ \mathbf{0} \\ \mathbf{F}_{10,n} \end{Bmatrix} \tag{18}$$

By condensing the internal DOFs, the equilibrium equation given in Eq. (18) relating only to nodes 7 and 10 can be obtained. For convenience, considering sub-cells 5, 6 and 7 to be the super-cell I, one can get the corresponding equilibrium equation as

$$\begin{bmatrix} \mathbf{D}_{LL,n}^{(\mathrm{I})} & \mathbf{D}_{LR,n}^{(\mathrm{I})} \\ \mathbf{D}_{RL,n}^{(\mathrm{I})} & \mathbf{D}_{RR,n}^{(\mathrm{I})} \end{bmatrix} \begin{Bmatrix} \mathbf{U}_{7,n} \\ \mathbf{U}_{10,n} \end{Bmatrix} = \begin{Bmatrix} \mathbf{F}_{7,n} \\ \mathbf{F}_{10,n} \end{Bmatrix} \tag{19}$$

where

$$\begin{aligned} \begin{bmatrix} \mathbf{D}_{LL,n}^{(\mathrm{I})} & \mathbf{D}_{LR,n}^{(\mathrm{I})} \\ \mathbf{D}_{RL,n}^{(\mathrm{I})} & \mathbf{D}_{RR,n}^{(\mathrm{I})} \end{bmatrix} &= \begin{bmatrix} \mathbf{D}_{LL,n}^{(5)} & \mathbf{D}_{LR,n}^{(5)} \\ \mathbf{0} & \mathbf{0} \end{bmatrix} \\ &\quad - \begin{bmatrix} \mathbf{0} & \mathbf{0} \\ \mathbf{D}_{RL,n}^{(7)} & \mathbf{D}_{RR,n}^{(7)} \end{bmatrix} \begin{bmatrix} \mathbf{D}_{LR,n}^{(6)} & \mathbf{0} \\ \mathbf{D}_{RR,n}^{(6)} + \mathbf{D}_{LL,n}^{(7)} & \mathbf{D}_{LR,n}^{(7)} \end{bmatrix}^{-1} \begin{bmatrix} \mathbf{D}_{RL,n}^{(5)} & \mathbf{D}_{RR,n}^{(5)} + \mathbf{D}_{LL,n}^{(6)} \\ \mathbf{0} & \mathbf{D}_{RL,n}^{(6)} \end{bmatrix} \end{aligned} \tag{20}$$

Substituting Eqs. (1), (4) and (7) into Eq. (19) to express $\mathbf{U}_{7,\mathrm{n}}$ and $\mathbf{U}_{10,n}$ in terms of $\mathbf{U}_{5,n}$ and $\mathbf{U}_{6,n}$, respectively, and pre-multiplying both sides of resultant equations by $\mathbf{Q}_2{}^{\mathrm{T}}$, this yields,

$$\begin{bmatrix} \mathbf{Q}_2{}^{\mathrm{T}}\mathbf{D}_{LL,n}^{(\mathrm{I})}\mathbf{Q}_2 & \mathbf{Q}_2{}^{\mathrm{T}}\mathbf{D}_{LR,n}^{(\mathrm{I})}\mathbf{Q}_2 \\ \mathbf{Q}_2{}^{\mathrm{T}}\mathbf{D}_{RL,n}^{(\mathrm{I})}\mathbf{Q}_2 & \mathbf{Q}_2{}^{\mathrm{T}}\mathbf{D}_{RR,n}^{(\mathrm{I})}\mathbf{Q}_2 \end{bmatrix} \begin{Bmatrix} \mathbf{U}_{5,n} \\ \mathbf{U}_{6,n} \end{Bmatrix} = \begin{Bmatrix} \mathbf{Q}_2{}^{\mathrm{T}}\mathbf{F}_{7,n} \\ \mathbf{Q}_2{}^{\mathrm{T}}\mathbf{F}_{10,n} \end{Bmatrix} \tag{21}$$

Similarly, sub-cells 8, 9 and 10 shown in Fig. 3 are combined into the super-cell II, and the equilibrium equations relating nodes 9 and 12 can be obtained as

$$\begin{bmatrix} \mathbf{D}_{LL,n}^{(\mathrm{II})} & \mathbf{D}_{LR,n}^{(\mathrm{II})} \\ \mathbf{D}_{RL,n}^{(\mathrm{II})} & \mathbf{D}_{RR,n}^{(\mathrm{II})} \end{bmatrix} \begin{Bmatrix} \mathbf{U}_{9,n} \\ \mathbf{U}_{12,n} \end{Bmatrix} = \begin{Bmatrix} \mathbf{F}_{9,n} \\ \mathbf{F}_{12,n} \end{Bmatrix} \tag{22}$$

The displacement vectors $\mathbf{U}_{9,n}$ and $\mathbf{U}_{12,n}$ can also be represented by $\mathbf{U}_{5,n}$ and $\mathbf{U}_{6,n}$, respectively, by substituting Eqs. (3), (4) and (7) into Eq. (22), and this leads to the following equilibrium equations

$$\begin{bmatrix} \mathbf{Q}_1{}^{\mathrm{T}}\mathbf{D}_{LL,n}^{(\mathrm{II})}\mathbf{Q}_1 & \mathbf{Q}_1{}^{\mathrm{T}}\mathbf{D}_{LR,n}^{(\mathrm{II})}\mathbf{Q}_1 \\ \mathbf{Q}_1{}^{\mathrm{T}}\mathbf{D}_{RL,n}^{(\mathrm{II})}\mathbf{Q}_1 & \mathbf{Q}_1{}^{\mathrm{T}}\mathbf{D}_{RR,n}^{(\mathrm{II})}\mathbf{Q}_1 \end{bmatrix} \begin{Bmatrix} \mathbf{U}_{5,n} \\ \mathbf{U}_{6,n} \end{Bmatrix} = \begin{Bmatrix} \mathbf{Q}_1{}^{\mathrm{T}}\mathbf{F}_{9,n} \\ \mathbf{Q}_1{}^{\mathrm{T}}\mathbf{F}_{12,n} \end{Bmatrix} \tag{23}$$

By assembling the dynamic stiffness matrices of all sub-cells and super-cells, i.e., Eqs. (11), (12), (13), (14), (21) and (23), after some manipulations, the equilibrium equations of the entire periodic cell can be given by

$$\begin{bmatrix} \mathbf{A}_{11} & \mathbf{A}_{12} & 0 & 0 & 0 & 0 \\ \mathbf{A}_{21} & \mathbf{A}_{22} & \mathbf{A}_{23} & 0 & \mathbf{A}_{25} & 0 \\ 0 & \mathbf{A}_{32} & \mathbf{A}_{33} & 0 & 0 & 0 \\ 0 & 0 & 0 & \mathbf{A}_{44} & \mathbf{A}_{45} & 0 \\ 0 & \mathbf{A}_{52} & 0 & \mathbf{A}_{54} & \mathbf{A}_{55} & \mathbf{A}_{56} \\ 0 & 0 & 0 & 0 & \mathbf{A}_{65} & \mathbf{A}_{66} \end{bmatrix} \begin{Bmatrix} \mathbf{U}_{1,n} \\ \mathbf{U}_{5,n} \\ \mathbf{U}_{3,n} \\ \mathbf{U}_{4,n} \\ \mathbf{U}_{6,n} \\ \mathbf{U}_{2,n} \end{Bmatrix} = \begin{Bmatrix} \mathbf{F}_{1,n} \\ \mathbf{0} \\ \mathbf{0} \\ \mathbf{0} \\ \mathbf{0} \\ \mathbf{F}_{2,n} \end{Bmatrix} \tag{24}$$

where

$$\mathbf{A}_{11} = \mathbf{D}_{LL,n}^{(1)},\ \mathbf{A}_{12} = \mathbf{D}_{LR,n}^{(1)},\ \mathbf{A}_{21} = \mathbf{D}_{RL,n}^{(1)}$$

$$\mathbf{A}_{22} = \mathbf{D}_{RR,n}^{(1)} + \mathbf{D}_{LL,n}^{(3)} + \mathbf{Q}_2{}^{\mathrm{T}}\mathbf{D}_{LL,n}^{(\mathrm{I})}\mathbf{Q}_2 + \mathbf{Q}_1{}^{\mathrm{T}}\mathbf{D}_{LL,n}^{(\mathrm{II})}\mathbf{Q}_1$$

$$\mathbf{A}_{23} = \mathbf{D}_{LR,n}^{(3)},\quad \mathbf{A}_{25} = \mathbf{Q}_2{}^{\mathrm{T}}\mathbf{D}_{LR,n}^{(\mathrm{I})}\mathbf{Q}_2 + \mathbf{Q}_1{}^{\mathrm{T}}\mathbf{D}_{LR,n}^{(\mathrm{II})}\mathbf{Q}_1$$

$$\mathbf{A}_{32} = \mathbf{D}_{RL,n}^{(3)},\ \mathbf{A}_{33} = \mathbf{D}_{RR,n}^{(3)},\ \mathbf{A}_{44} = \mathbf{D}_{LL,n}^{(4)},\ \mathbf{A}_{45} = \mathbf{D}_{LR,n}^{(4)}$$

$$\mathbf{A}_{52} = \mathbf{Q}_2{}^{\mathrm{T}}\mathbf{D}_{RL,n}^{(\mathrm{I})}\mathbf{Q}_2 + \mathbf{Q}_1{}^{\mathrm{T}}\mathbf{D}_{RL,n}^{(\mathrm{II})}\mathbf{Q}_1,\ \mathbf{A}_{54} = \mathbf{D}_{RL,n}^{(4)}$$

$$\mathbf{A}_{55} = \mathbf{D}_{LL,n}^{(2)} + \mathbf{D}_{RR,n}^{(4)} + \mathbf{Q}_2{}^{\mathrm{T}}\mathbf{D}_{RR,n}^{(\mathrm{I})}\mathbf{Q}_2 + \mathbf{Q}_1{}^{\mathrm{T}}\mathbf{D}_{RR,n}^{(\mathrm{II})}\mathbf{Q}_1$$

$$\mathbf{A}_{56} = \mathbf{D}_{LR,n}^{(2)},\ \mathbf{A}_{65} = \mathbf{D}_{RL,n}^{(2)},\ \mathbf{A}_{66} = \mathbf{D}_{RR,n}^{(2)}$$

After condensing the internal DOFs, the following dynamic equilibrium equations relating nodes 1 and 2 of the periodic cell is given by

$$\mathbf{D}_n \begin{Bmatrix} \mathbf{U}_{1,n} \\ \mathbf{U}_{2,n} \end{Bmatrix} = \begin{bmatrix} \mathbf{D}_{LL,n} & \mathbf{D}_{LR,n} \\ \mathbf{D}_{RL,n} & \mathbf{D}_{RR,n} \end{bmatrix} \begin{Bmatrix} \mathbf{U}_{1,n} \\ \mathbf{U}_{2,n} \end{Bmatrix} = \begin{Bmatrix} \mathbf{F}_{1,n} \\ \mathbf{F}_{2,n} \end{Bmatrix} \tag{25}$$

where, $\mathbf{U}_{1,n}$, $\mathbf{U}_{2,n}$ and $\mathbf{F}_{1,n}$, $\mathbf{F}_{2,n}$ are generalized displacement and force vectors at the left and right sides of the periodic cell. $\mathbf{D}_n \in \mathbb{R}^{6\times 6}$ is the condensed super-element DSM of the periodic cell including bolted flange joints, and

$$\begin{aligned} \begin{bmatrix} \mathbf{D}_{LL,n} & \mathbf{D}_{LR,n} \\ \mathbf{D}_{RL,n} & \mathbf{D}_{RR,n} \end{bmatrix} &= \begin{bmatrix} \mathbf{A}_{11} & \mathbf{A}_{12} \\ \mathbf{0} & \mathbf{0} \end{bmatrix} \\ &- \begin{bmatrix} \mathbf{0} & \mathbf{0} & \mathbf{0} & \mathbf{0} \\ \mathbf{0} & \mathbf{0} & \mathbf{A}_{65} & \mathbf{A}_{66} \end{bmatrix} \begin{bmatrix} \mathbf{A}_{23} & \mathbf{0} & \mathbf{A}_{25} & \mathbf{0} \\ \mathbf{A}_{33} & \mathbf{0} & \mathbf{0} & \mathbf{0} \\ \mathbf{0} & \mathbf{A}_{44} & \mathbf{A}_{45} & \mathbf{0} \\ \mathbf{0} & \mathbf{A}_{54} & \mathbf{A}_{55} & \mathbf{A}_{56} \end{bmatrix}^{-1} \begin{bmatrix} \mathbf{A}_{21} & \mathbf{A}_{22} \\ \mathbf{0} & \mathbf{A}_{32} \\ \mathbf{0} & \mathbf{0} \\ \mathbf{0} & \mathbf{A}_{52} \end{bmatrix} \end{aligned} \tag{26}$$

For the entire periodic system, rewrite Eq. (25) for the jth ($j = 1,2,\cdots,N_P$) cell as

$$\begin{bmatrix} \mathbf{D}_{LL,n}^{[j]} & \mathbf{D}_{LR,n}^{[j]} \\ \mathbf{D}_{RL,n}^{[j]} & \mathbf{D}_{RR,n}^{[j]} \end{bmatrix} \begin{Bmatrix} \mathbf{U}_{L,n}^{[j]} \\ \mathbf{U}_{R,n}^{[j]} \end{Bmatrix} = \begin{Bmatrix} \mathbf{F}_{L,n}^{[j]} \\ \mathbf{F}_{R,n}^{[j]} \end{Bmatrix} \tag{27}$$

where N_P denotes the number of cells in the periodically supported beams. $\mathbf{D}_{LL,n}^{[j]}$, $\mathbf{D}_{LR,n}^{[j]}$, $\mathbf{D}_{RL,n}^{[j]}$ and $\mathbf{D}_{RR,n}^{[j]}$ are the partitioned matrices of the condensed super-element DSM $\mathbf{D}_n^{[j]}$ with respect to the jth cell. For consistence, the subscripts 1 and 2 in the generalized displacement and force vectors are reassigned as L and R hereafter, respectively.

For convenience, Eq. (27) can be further reassembled as:

$$\mathbf{Y}_{R,n}^{[j]} = \mathbf{T}_n^{[j]} \mathbf{Y}_{L,n}^{[j]} \tag{28}$$

where $\mathbf{Y}_{L,n}^{[j]}$ and $\mathbf{Y}_{R,n}^{[j]}$ are the state vectors on the right and left ends of the jth cell, respectively, i.e.,

$$\mathbf{Y}_{L,n}^{[j]} = \begin{Bmatrix} \mathbf{U}_{L,n}^{[j]} \\ \mathbf{F}_{L,n}^{[j]} \end{Bmatrix}, \quad \mathbf{Y}_{R,n}^{[j]} = \begin{Bmatrix} \mathbf{U}_{R,n}^{[j]} \\ \mathbf{F}_{R,n}^{[j]} \end{Bmatrix} \tag{29}$$

and the transformation matrix $\mathbf{T}_n^{[j]}$ relating the state vectors at both ends of the jth cell is given by

$$\mathbf{T}_n^{[j]} = \begin{bmatrix} -\left(\mathbf{D}_{LR,n}^{[j]}\right)^{-1}\mathbf{D}_{LL,n}^{[j]} & \left(\mathbf{D}_{LR,n}^{[j]}\right)^{-1} \\ \mathbf{D}_{RL,n}^{[j]} - \mathbf{D}_{RR,n}^{[j]}\left(\mathbf{D}_{LR,n}^{[j]}\right)^{-1}\mathbf{D}_{LL,n}^{[j]} & \mathbf{D}_{RR,n}^{[j]}\left(\mathbf{D}_{LR,n}^{[j]}\right)^{-1} \end{bmatrix} \tag{30}$$

Moreover, the continuity and compatibility conditions at the jth interface require continuity of generalized displacements and forces at the right end of the jth cell and left end of the $(j+1)$th one. They are given, respectively, by

$$\mathbf{U}_{R,n}^{[j]} = \mathbf{U}_{L,n}^{[j+1]}, \quad \mathbf{F}_{R,n}^{[j]} = -\mathbf{F}_{L,n}^{[j+1]} \tag{31}$$

or in a matrix forms as

$$\mathbf{Y}_{R,n}^{[j]} = \begin{bmatrix} \mathbf{I}_{N_m} & 0 \\ 0 & -\mathbf{I}_{N_m} \end{bmatrix} \mathbf{Y}_{L,n}^{[j+1]} = \mathbf{\Lambda}\mathbf{Y}_{L,n}^{[j+1]} \tag{32}$$

where $\mathbf{I}_{N_m}$ is the N_m- by-N_m identity matrix.

Substituting Eq. (32) into Eq. (28) yields

$$\mathbf{Y}_{L,n}^{[j+1]} = \overline{\mathbf{T}}_n^{[j]}\mathbf{Y}_{L,n}^{[j]} \tag{33}$$

where $\overline{\mathbf{T}}_n^{[j]} = \mathbf{\Lambda}^{-1}\mathbf{T}_n^{[j]}$ is the transfer matrix from the left end of the jth cell to the left end of the $(j+1)$th one. Accordingly, the relationship between the state vectors at the left end of the first cell and the left end of the last one can be given by

$$\mathbf{Y}_{L,n}^{[N_P]} = \prod_{j=1}^{N_P-1} \overline{\mathbf{T}}_n^{[j]}\, \mathbf{Y}_{L,n}^{[1]} \tag{34}$$

The state vectors at the beginning and the end of entire periodic structural system can be further related by combining Eqs. (28) and (34) as

$$\mathbf{Y}_{R,n}^{[N_P]} = \mathbf{T}_n^{[N_P]}\mathbf{Y}_{L,n}^{[N_P]} = \mathbf{\Gamma}_n\mathbf{Y}_{L,n}^{[1]} \tag{35}$$

and

$$\mathbf{\Gamma}_n = \mathbf{T}_n^{[N_P]} \prod_{j=1}^{N_P-1} \overline{\mathbf{T}}_n^{[j]} \tag{36}$$

where $\mathbf{\Gamma}_n$ represents the system transfer matrix of whole periodic structure.

By noting the partition form of the system transfer matrix

$$\boldsymbol{\Gamma}_n = \begin{bmatrix} \boldsymbol{\Gamma}_{LL,n} & \boldsymbol{\Gamma}_{LR,n} \\ \boldsymbol{\Gamma}_{RL,n} & \boldsymbol{\Gamma}_{RR,n} \end{bmatrix} \tag{37}$$

the relationship between generalized displacement and force vectors at both ends of the entire periodic system can be obtained by rearranging Eq. (35) as

$$\mathbf{D}_n^G \begin{Bmatrix} \mathbf{U}_{L,n}^{[1]} \\ \mathbf{U}_{R,n}^{[N_P]} \end{Bmatrix} = \begin{Bmatrix} \mathbf{F}_{L,n}^{[1]} \\ \mathbf{F}_{R,n}^{[N_P]} \end{Bmatrix} \tag{38}$$

where $\mathbf{D}_n^G$ representing the system DSM of the entire periodically supported structure is given by

$$\mathbf{D}_n^G = \begin{bmatrix} -\boldsymbol{\Gamma}_{LR,n}^{-1}\boldsymbol{\Gamma}_{LL,n} & \boldsymbol{\Gamma}_{LR,n}^{-1} \\ \boldsymbol{\Gamma}_{RL,n} - \boldsymbol{\Gamma}_{RR,n}\boldsymbol{\Gamma}_{LR,n}^{-1}\boldsymbol{\Gamma}_{LL,n} & \boldsymbol{\Gamma}_{RR,n}\boldsymbol{\Gamma}_{LR,n}^{-1} \end{bmatrix} \tag{39}$$

For any specified frequency ω_n, if the forces applied to the two boundaries of the periodic structure are provided, the generalized displacements at both boundaries, i.e., $\mathbf{Y}_{L,n}^{[1]}$ and $\mathbf{Y}_{R,n}^{[N_P]}$, can be firstly derived with Eq. (38). Then, by further utilizing Eq. (33), the state vectors at two supports of an arbitrary cell (e.g., the kth cell) can be easily obtained as, respectively,

$$\begin{Bmatrix} \mathbf{Y}_{L,n}^{[k]} \\ \mathbf{Y}_{R,n}^{[k]} \end{Bmatrix} = \begin{Bmatrix} \prod_{j=1}^{k-1} \overline{\mathbf{T}}_n^{[j]}\, \mathbf{Y}_{L,n}^{[1]} \\ \mathbf{T}_n^{[k]} \prod_{j=1}^{k-1} \overline{\mathbf{T}}_n^{[j]}\, \mathbf{Y}_{L,n}^{[1]} \end{Bmatrix} \tag{40}$$

In addition, besides of the generalized displacements around pin supports, the proposed methodology can also be utilized to further obtain the generalized displacements at an arbitrary position in the periodic structure, e.g., the point *a* located within the kth cell as illustrated in Fig. 4. The main purpose is consistent with the general situation in real application as only the transverse responses can be conveniently measured through the mounted sensors away from the supports. To achieve this goal, the proposed solution procedure consists of two steps. Firstly, the state vectors at two ends of the kth cell are obtained in Eq. (40) by implementing the proposed methodology. The generalized forces $\mathbf{F}_{L,n}^{[k]}, \mathbf{F}_{R,n}^{[k]}$ and displacements $\mathbf{U}_{L,n}^{[k]}, \mathbf{U}_{R,n}^{[k]}$ at both ends of this cell can be extracted from the state vectors $\mathbf{Y}_{L,n}^{[k]}$ and $\mathbf{Y}_{R,n}^{[k]}$. Secondly, the kth cell is further subdivided into two new sub-cells, i.e., sub-cell k_1 and sub-cell k_2. Referring to Figs. 3 and 4, the former is a part of original sub-cell 1, and the latter including the bolted

flange joint represents the remaining part of the kth cell. By assembling the dynamic stiffness matrices of sub-cells k_1 and k_2, i.e., $\mathbf{D}_n^{[k_1]}$ and $\mathbf{D}_n^{[k_2]}$, and also employing the previously obtained force and displacement boundary conditions, the governing equation of the kth cell is formulated as

$$\begin{bmatrix} \mathbf{D}_{LL,n}^{[k_1]} & \mathbf{D}_{LR,n}^{[k_1]} & \\ \mathbf{D}_{RL,n}^{[k_1]} & \mathbf{D}_{RR,n}^{[k_1]} + \mathbf{D}_{LL,n}^{[k_2]} & \mathbf{D}_{LR,n}^{[k_2]} \\ & \mathbf{D}_{RL,n}^{[k_2]} & \mathbf{D}_{RR,n}^{[k_2]} \end{bmatrix} \begin{Bmatrix} \mathbf{U}_{L,n}^{[k]} \\ \mathbf{U}_{a,n}^{[k]} \\ \mathbf{U}_{R,n}^{[k]} \end{Bmatrix} = \begin{Bmatrix} \mathbf{F}_{L,n}^{[k]} \\ \mathbf{F}_{a,n}^{[k]} \\ \mathbf{F}_{R,n}^{[k]} \end{Bmatrix} \tag{41}$$

where $\mathbf{U}_{a,n}^{[k]}$ denotes the generalized displacement at the node *a*, and the partitioned matrices of dynamic stiffness matrices $\mathbf{D}_n^{[k_1]}$ and $\mathbf{D}_n^{[k_2]}$ are also employed.

Thus, the generalized displacement at the intermediate node *a* of the kth cell $\mathbf{U}_{a,n}^{[k]}$ can be obtained from Eq. (41) as:

$$\mathbf{U}_{a,n}^{[k]} = \left(\mathbf{D}_{RR,n}^{[k_1]} + \mathbf{D}_{LL,n}^{[k_2]}\right)^{-1} \left(\mathbf{F}_{a,n}^{[k]} - \mathbf{D}_{RL,n}^{[k_1]}\mathbf{U}_{L,n}^{[k]} - \mathbf{D}_{LR,n}^{[k_2]}\mathbf{U}_{R,n}^{[k]}\right) \tag{42}$$

where, it is noted that the generalized force $\mathbf{F}_{a,n}^{[k]}$ should vanish due to the internal equilibrium condition at the specified point *a*, and the above equation can be further simplified as

$$\mathbf{U}_{a,n}^{[k]} = -\left(\mathbf{D}_{RR,n}^{[k_1]} + \mathbf{D}_{LL,n}^{[k_2]}\right)^{-1} \left(\mathbf{D}_{RL,n}^{[k_1]}\mathbf{U}_{L,n}^{[k]} + \mathbf{D}_{LR,n}^{[k_2]}\mathbf{U}_{R,n}^{[k]}\right) \tag{43}$$

In the same manner, the generalized displacements with respect to the given number of intermediate nodes $\mathbf{U}_{a_p,n}^{[k]}$ $(p = 1,2,\dots,N_O)$ corresponding to the sensors distributed along the periodically supported structural systems can be obtained by the proposed procedure, and N_O is the number of measurement points.

It is should be pointed out that, by eliminating the longitudinal displacement components from the system DSM $\mathbf{D}_n$ given in Eq. (25), a reduced-order DSM can be derived in order to be consistent with the employed Euler-Bernoulli beam theory. By further considering the support condition of cell boundary in the present periodically supported structural system, the resulting dynamic equilibrium equation actually relates the bending moment to the rotation at both ends of cell. In addition, it is also noted that since the generalized displacement responses are obtained in frequency-domain, which cannot readily be utilized in the proposed detection methodology as introduced below, and the first jth natural frequencies and mode shapes of the periodic structural system can be achieved following the proposed strategy given in the flowchart as shown in Fig. 5.

2.2 Phase I: Bayesian model class selection

The goal in the first phase of the proposed detection methodology is to use a given set of measurement data $\mathcal{D}$ to select the most plausible class of models representing the system out of N_C prescribed classes of models. In the present study, data $\mathcal{D}$ consists of N_r sets of measured natural frequencies and mode shapes of the first N_m modes, i.e.,

$$\mathcal{D} \overset{\text{def}}{=} \bigcup_{r=1}^{N_r} \left\{ \left(\tilde{f}_1^{(r)}, \tilde{\boldsymbol{\Phi}}_1^{(r)} \right), \left(\tilde{f}_2^{(r)}, \tilde{\boldsymbol{\Phi}}_2^{(r)} \right), \cdots, \left(\tilde{f}_{N_m}^{(r)}, \tilde{\boldsymbol{\Phi}}_{N_m}^{(r)} \right) \right\} \tag{44}$$

where $\tilde{f}_m^{(r)}, \tilde{\boldsymbol{\Phi}}_m^{(r)} \in \mathbb{R}^{No \times 1}$ represent the mth ($m = 1,2,\cdots,N_m$) natural frequency and mode shape with respect to the rth ($r = 1,2,\cdots,N_r$) set of measurement, respectively. The superscript $\tilde{}$ denotes the measured quantities.

The Bayesian model class selection method [50,51] is adopted to select the "optimal" model class for the purpose of bolt loosening detection in the periodically supported structural system. In this section, the related theories of the Bayesian model class selection method are only briefly reviewed due to the limited space. Interested readers are directed to reference [50] for the detailed information. To select the most plausible model class among N_C given model classes $\mathcal{C}_1, \mathcal{C}_2, \cdots, \mathcal{C}_{N_C}$, the probability of a class of models conditional on the given set of measured data $\mathcal{D}$ can be obtained based on Bayes' theorem by:

$$p(\mathcal{C}_j|\mathcal{D},\mathcal{U}) = \frac{p(\mathcal{D}|\mathcal{C}_j,\mathcal{U})p(\mathcal{C}_j|\mathcal{U})}{\sum_{j=1}^{N_c} p(\mathcal{D}|\mathcal{C}_j,\mathcal{U})\, p(\mathcal{C}_j|\mathcal{U})} \tag{45}$$

where $\mathcal{U}$ represents the user's judgment on the initial plausibility of the given model class. The prior probability $p(\mathcal{C}_j|\mathcal{U})$ on the model class $\mathcal{C}_j$, for $j = 1$ to N_C, satisfies $\sum_{j=1}^{N_c} p(\mathcal{C}_j|\mathcal{U}) = 1$. Since there is generally no prior information about each class of models for the purpose of damage identification, and it's simply assumed hereafter that each individual model class possesses the same initial plausibility, i.e., $p(\mathcal{C}_j|\mathcal{U}) = 1/N_C$. The factor $p(\mathcal{D}|\mathcal{C}_j,\mathcal{U})$ is the most important term in Eq. (45), and it is known as the evidence for the model class $\mathcal{C}_j$ providing the set of dynamic measurements $\mathcal{D}$. Generally, the class of models to be used is the one that maximizes the probability $p(\mathcal{C}_j|\mathcal{D},\mathcal{U})$, i.e., maximizes the evidence $p(\mathcal{D}|\mathcal{C}_j,\mathcal{U})$ with respect to $\mathcal{C}_j$ equivalently. When applying the Bayesian model class selection method to identify the most probable model class, it's assumed $\mathcal{C}_j$ alone specifies the probability density function (PDF) for the data $\mathcal{D}$, and $\mathcal{U}$ is thus dropped in $p(\mathcal{D}|\mathcal{C}_j,\mathcal{U})$ hereunder.

For the globally identifiable cases [52,53], the posterior PDF of $\boldsymbol{\theta}_j$ for a given set of measured data $\mathcal{D}$, can be approximated by a Gaussian distribution, and the evidence $p(\mathcal{D}|\mathcal{C}_j)$ can thus be asymptotically approximated as [50,54]

$$p(\mathcal{D}|\mathcal{C}_j) \approx p(\mathcal{D}|\widehat{\boldsymbol{\theta}}_j, \mathcal{C}_j) p(\widehat{\boldsymbol{\theta}}_j|\mathcal{C}_j) (2\pi)^{\frac{N_j}{2}} \left|\mathbf{H}_j(\widehat{\boldsymbol{\theta}}_j)\right|^{-\frac{1}{2}} \tag{46}$$

where $\boldsymbol{\theta}_j \in \mathbb{R}^{N_j \times 1}$ is the parameter vector of the jth class of models $\mathcal{C}_j$ in the prescribed parameter space. N_j is the number of uncertain parameters in $\boldsymbol{\theta}_j$. $\widehat{\boldsymbol{\theta}}_j$ is the most probable model parameters in model class $\mathcal{C}_j$, and $\mathbf{H}_j(\widehat{\boldsymbol{\theta}}_j)$ is the Hessian matrix of the function $-\ln[p(\mathcal{D}|\boldsymbol{\theta}_j, \mathcal{C}_j) p(\boldsymbol{\theta}_j|\mathcal{C}_j)]$ with respect to $\boldsymbol{\theta}_j$ evaluated at $\widehat{\boldsymbol{\theta}}_j$, which is calculated numerically by using the finite difference method. The evidence in Eq. (45) consists of two terms, i.e., the likelihood factor $p(\mathcal{D}|\widehat{\boldsymbol{\theta}}_j, \mathcal{C}_j)$ and the Ockham factor $p(\widehat{\boldsymbol{\theta}}_j|\mathcal{C}_j)(2\pi)^{N_j/2}\left|\mathbf{H}_j(\widehat{\boldsymbol{\theta}}_j)\right|^{-1/2}$. Specifically, the likelihood factor favors model classes with more uncertain parameters. Thus it will be higher for those model classes making the probability of the data $\mathcal{D}$ higher, implying a better fit to the data. The Ockham factor, however, imposes a penalty against the complexity of the specified model class. The balance between these two factors allows one to select the most probable model class through a mathematically rigorous and robust way, which is just complex enough to fit the given measured data. In this study, the class of models to be selected is the one possessing the highest value of evidence among the entire set of model classes for the given set of measured data.

2.3 Phase II: Partial filter-based damage identification

Provided the most plausible model class $\mathcal{C}_l$ $(l = 1,2,\cdots,N_C)$ identified in the previous phase, the main objective of this phase is to develop a procedure based on dynamic state estimation methods to calculate the posterior PDF of the uncertain model parameters $\boldsymbol{\theta}_l$ for a given set of measured data $\mathcal{D}$. The subscripts l in the symbols of model class and model parameter vector are dropped in the following formulation to simplify the expressions. Following the framework of dynamic state estimation, a nonlinear dynamical system for model class $\mathcal{C}$ can be given as

$$\boldsymbol{\theta}^{(k)} = \mathcal{F}(\boldsymbol{\theta}^{(k-1)}; \mathcal{C}) + \mathbf{u}^{(k-1)} \tag{47}$$

$$\mathcal{D}^{(k)} = \mathcal{G}(\boldsymbol{\theta}^{(k)}; \mathcal{C}) + \mathbf{v}^{(k)} \tag{48}$$

where $\boldsymbol{\theta}^{(k)}$ is the state vector of the dynamical system at time k, and $\mathcal{D}^{(k)}$ is the measurement vector at time k. $\mathcal{F}(\cdot)$ is the prescribed state transition function, and $\mathcal{G}(\cdot)$ is the

measurement function. $\mathbf{u}^{(k)}$ and $\mathbf{v}^{(k)}$ are the independent identically distributed random noises in the system process and measurement process accordingly.

Denoting $\boldsymbol{\theta}^{(0:k)} = \{\boldsymbol{\theta}^{(0)}, \boldsymbol{\theta}^{(1)}, \dots, \boldsymbol{\theta}^{(k)}\}$ and $\mathcal{D}^{(1:k)} = \{\mathcal{D}^{(1)}, \mathcal{D}^{(2)}, \dots, \mathcal{D}^{(k)}\}$ as the sequence up to time k of state vectors and measurements, respectively, from a Bayesian perspective, the construction of the posterior PDF $p(\boldsymbol{\theta}^{(k)}|\mathcal{D}^{(1:k)}, \mathcal{C})$ requires to recursively calculate some degree of belief in the state $\boldsymbol{\theta}^{(k)}$ at time k for the class of models $\mathcal{C}$, given the data $\mathcal{D}^{(1:k)}$ up to time *k*. It is assumed that the prior distribution $p(\boldsymbol{\theta}^{(0)}|\mathcal{C})$ of the state vector is available, and the PDF $p(\boldsymbol{\theta}^{(k)}|\mathcal{D}^{(1:k)}, \mathcal{C})$ can be obtained through two successive stages, i.e., the prediction stage and subsequent updating stage.

Providing the PDF $p(\boldsymbol{\theta}^{(k-1)}|\mathcal{D}^{(1:k-1)}, \mathcal{C})$ at time $k-1$, the prediction stage involves the utilization of the system model to obtain the prior PDF of the state at time k via the Chapman–Kolmogorov equation:

$$p(\boldsymbol{\theta}^{(k)}|\mathcal{D}^{(1:k-1)}, \mathcal{C}) = \int p(\boldsymbol{\theta}^{(k)}|\boldsymbol{\theta}^{(k-1)}, \mathcal{C}) p(\boldsymbol{\theta}^{(k-1)}|\mathcal{D}^{(1:k-1)}, \mathcal{C}) \, \mathrm{d}\boldsymbol{\theta}^{(k-1)} \tag{49}$$

The probabilistic model of the state transition $p(\boldsymbol{\theta}^{(k)}|\boldsymbol{\theta}^{(k-1)}, \mathcal{C})$ is defined by the state transition function and the known statistics of $\mathbf{u}^{(k-1)}$ in Eq. (47) as

$$p(\boldsymbol{\theta}^{(k)}|\boldsymbol{\theta}^{(k-1)}, \mathcal{C}) = \int p(\boldsymbol{\theta}^{(k)}|\boldsymbol{\theta}^{(k-1)}, \mathbf{u}^{(k-1)}, \mathcal{C}) p(\mathbf{u}^{(k-1)}|\boldsymbol{\theta}^{(k-1)}, \mathcal{C}) \, \mathrm{d}\mathbf{u}^{(k-1)} \tag{50}$$

In the updating stage, by using the Bayes' theorem, the posterior distribution of $\boldsymbol{\theta}^{(k)}$ is obtained through the correction of the prior in Eq. (49) when a new set of measurement $\mathcal{D}^{(k)}$ is available at time k:

$$p(\boldsymbol{\theta}^{(k)}|\mathcal{D}^{(1:k)}, \mathcal{C}) = \frac{p(\mathcal{D}^{(k)}|\boldsymbol{\theta}^{(k)}, \mathcal{C}) p(\boldsymbol{\theta}^{(k)}|\mathcal{D}^{(1:k-1)}, \mathcal{C})}{p(\mathcal{D}^{(k)}|\mathcal{D}^{(1:k-1)})} \tag{51}$$

where the conditional PDF $p(\mathcal{D}^{(k)}|\boldsymbol{\theta}^{(k)}, \mathcal{C})$ is defined through both the measurement function and the known statistics of $\mathbf{v}^{(k)}$ as

$$p(\mathcal{D}^{(k)}|\boldsymbol{\theta}^{(k)}, \mathcal{C}) = \int p(\mathcal{D}^{(k)}|\boldsymbol{\theta}^{(k)}, \mathbf{v}^{(k)}, \mathcal{C}) p(\mathbf{v}^{(k)}|\boldsymbol{\theta}^{(k)}, \mathcal{C}) \, \mathrm{d}\mathbf{v}^{(k)} \tag{52}$$

The procedure of exact Bayesian solution for calculating the posterior PDF $p(\boldsymbol{\theta}^{(k)}|\mathcal{D}^{(1:k)}, \mathcal{C})$ is summarized above through Eqs. (49) to (52). However, it should be realized that due to the evaluation of the complex high-dimensional integrals involved in these formulas, it is extremely difficult, if not impossible, for these formulas to be utilized analytically to obtain the

conditional distribution except for a few cases, such as the linear Gaussian space models. In such circumstances, it is more favorable for adopting Monte Carlo simulation-based methods, such as the particle filter approach [55], to provide an approximation of the posterior distribution $p\left(\boldsymbol{\theta}^{(k)}\middle|\mathcal{D}^{(1:k)},\mathcal{C}\right)$ by using a set of support points $\boldsymbol{\theta}_i^{(k)}$, $i=1,2,\dots,N_s$, with associated importance weight $w_i^{(k)}$. Thus, the posterior PDF can be approximated in a weighted form as:

$$p\left(\boldsymbol{\theta}^{(k)}\middle|\mathcal{D}^{(1:k)},\mathcal{C}\right)\approx\sum_{i=1}^{N_s}w_i^{(k)}\delta\left(\boldsymbol{\theta}^{(k)}-\boldsymbol{\theta}_i^{(k)}\right) \tag{53}$$

where δ stands for the Dirac-delta function and the importance weight $w_i^{(k)}$ is determined by using importance sampling approach, and the weights are normalized so that their sum is equal to unity. Since it is usually impossible to sample from the true posterior, it is more convenient to sample from an easy-to-implement distribution, the importance density function denoted by $q\left(\boldsymbol{\theta}_i^{(k)}\middle|\mathcal{D}^{(1:k)},\mathcal{C}\right)$, from which the N_s samples $\boldsymbol{\theta}_i^{(k)}$ are drawn.

By utilizing the state-space assumptions and assuming the particles $\boldsymbol{\theta}_i^{(0:k-1)}$ and past measurements $\mathcal{D}^{(1:k-1)}$ are not concerned in the importance density function, the importance weight can be estimated recursively by [56]:

$$w_i^{(k)}\propto w_i^{(k-1)}\frac{p\left(\mathcal{D}^{(k)}\middle|\boldsymbol{\theta}_i^{(k)},\mathcal{C}\right)p\left(\boldsymbol{\theta}_i^{(k)}\middle|\boldsymbol{\theta}_i^{(k-1)},\mathcal{C}\right)}{q\left(\boldsymbol{\theta}_i^{(k)}\middle|\boldsymbol{\theta}_i^{(k-1)},\mathcal{D}^{(k)},\mathcal{C}\right)} \tag{54}$$

where the two terms in the numerator representing transitional density and likelihood function are defined in Eqs. (50) and (52), respectively. In practice, the importance density function is usually chosen as the transitional prior for simplicity, which yields

$$w_i^{(k)}\propto w_i^{(k-1)}p\left(\mathcal{D}^{(k)}\middle|\boldsymbol{\theta}_i^{(k)},\mathcal{C}\right) \tag{55}$$

It should be emphasized that the degeneracy of particles has an appreciable effect on the performance of the particle filter approach, making the approximation of the target distribution $p\left(\boldsymbol{\theta}^{(k)}\middle|\mathcal{D}^{(1:k)},\mathcal{C}\right)$ to be very poor with huge computational consumption on updating particles with minimum relevance. For eliminating of degeneracy, a resampling strategy is employed by regenerating particles from the approximate posterior distribution with equal weights, i.e., $w_i^{(k)}=1/N_s$, and a common measure of degeneracy of particles is the effective sample size given by [57]:

$$N_{eff} = 1/\sum_{i}^{N_s}\left(w_i^{(k)}\right)^2 \tag{56}$$

The resampling strategy aiming at discarding those particles with negligible weights and enhances the ones with larger weights. It takes place when the effective sample size N_{eff} falls below some user-defined threshold N_T. The flowchart of the proposed particle filter-based bolt-loosening detection is illustrated in Fig. 6.

It should be pointed out that, in the present study, the state vector $\boldsymbol{\theta}$, i.e., the uncertain model parameters, are assumed to be time invariant, and thus k represents an iteration number instead of a discrete time step. Accordingly, the process equation (i.e., Eq. (47)) within the framework of dynamic state estimation can be reformulated as

$$\boldsymbol{\theta}^{(k)} = \boldsymbol{\theta}^{(k-1)} + \mathbf{u}^{(k-1)} \tag{57}$$

where the artificial evolution noise $\mathbf{u}^{(k-1)} \in \mathbb{R}^{N_j \times 1}$ is assumed to be independent and identically distributed for all iterations, and the involvement of this noise term avoids the samples of $\boldsymbol{\theta}^{(k)}$ to get frozen around their initial estimations efficiently.

It is also assumed that the set of measurement data $\mathcal{D}^{(k)}$ in the observation equation (seeing Eq. (48)) are independent of the iteration number k and kept to be the same as $\mathcal{D}$ given in Eq. (44) during the iteration loops for the problem investigated in this paper. The measurement can be related to the state vector $\boldsymbol{\theta}^{(k)}$ through the implicit nonlinear measurement function defined in the following likelihood:

$$p\left(\mathcal{D}\middle|\boldsymbol{\theta}^{(k)}, \mathcal{C}\right) = (2\pi\sigma^2)^{-\frac{N_r N_m}{2}} \exp\left[-\frac{N_r N_m}{2\sigma^2}\mathcal{J}(\boldsymbol{\theta}^{(k)}; \mathcal{D}, \mathcal{C})\right] \tag{58}$$

where σ represents the standard deviation of the prediction error, which is defined as the difference between the measured and model-predicted outputs. $\mathcal{J}(\boldsymbol{\theta}^{(k)}; \mathcal{D}, \mathcal{C})$ is a positive definite measure-of-fit function given by

$$\mathcal{J}(\boldsymbol{\theta}^{(k)}; \mathcal{D}, \mathcal{C}) = \frac{1}{N_r N_m}\sum_{r=1}^{N_r}\sum_{m=1}^{N_m}\left[\left(\frac{f_m\left(\boldsymbol{\theta}^{(k)}; \mathcal{C}\right) - \tilde{f}_m^{(r)}}{\tilde{f}_m^{(r)}}\right)^2 + \frac{\boldsymbol{\phi}_m\left(\boldsymbol{\theta}^{(k)}; \mathcal{C}\right)^{\mathrm{T}}\left(\mathbf{I}_{N_O} - \tilde{\boldsymbol{\Phi}}_m^{(r)}\tilde{\boldsymbol{\Phi}}_m^{(r)^{\mathrm{T}}}\right)\boldsymbol{\phi}_m\left(\boldsymbol{\theta}^{(k)}; \mathcal{C}\right)}{\beta\|\boldsymbol{\phi}_m(\boldsymbol{\theta}^{(k)}; \mathcal{C})\|^2}\right] \tag{59}$$

where $f_m\left(\boldsymbol{\theta}^{(k)};\mathcal{C}\right)$ and $\boldsymbol{\phi}_m(\boldsymbol{\theta}^{(k)};\mathcal{C})$ represent the mth predicted natural frequencies and mode shape vectors with model class $\mathcal{C}$ parameterized by vector $\boldsymbol{\theta}^{(k)}$. $\mathbf{I}_{N_O}$ is the N_O-by-N_O identity matrix. β is the ratio between the prediction-error variances of mode shape vectors and natural frequencies [58]. It is assumed herein that the measured mode shapes are normalized so that its Euclidean norm $\left\|\tilde{\boldsymbol{\phi}}_m^{(r)}\right\|$ is equal to unity. Thus, through the above procedure, the posterior PDF $p\left(\boldsymbol{\theta}^{(k)}\middle|\mathcal{D}^{(1:k)},\mathcal{C}\right)$ in Eq. (53) can be obtained.

3. NUMERICAL SIMULATION

In this section, numerical simulation is conducted for a periodically supported beam endowed with bolted flange connections as shown in Fig. 7 to verify the proposed methodology. It is to be recalled that that the beam segment with flange joints between two adjacent supports is treated as the periodic cell within the concept of periodic structural system. In such circumstances, the total number of cells contained in this periodic system is $N_P = 10$, and these cells are assigned as a sequence number starting at 1 from the leftmost span to the rightmost one as indicated in Fig. 1 for convenience. The geometric and material properties of structure are shown in Table 1.

In order to verify the validity of the proposed transfer matrix-based method for calculating the dynamic response from an arbitrarily given point in the periodic structural system, the transverse and rotational displacements in frequency domain of node *a*, which is assumed to be 0.26m left from the second support as shown in Figs. 4 and 7, are calculated by applying a transient bending moment at the left end of the periodic system. The comparison results by assembling the DSM of each cell following the conventional global assembly method with the proposed transfer matrix-based method are illustrated in Fig. 8. It is very clear that the results obtained from the two methods completely match with each other, which demonstrates the accuracy of the proposed method.

In addition, it should be emphasized that the significant advantages of the proposed modelling method lies in its reduced-order form of system DSM, which is expected to reduce the computational cost to a large extent. To compare the efficiency of proposed solution method with the global assembly method for dynamic analysis of periodic structures, Fig. 9 shows the time used for calculating the transverse response at the arbitrary node a (seeing Fig. 7) with increasing number of cells (N_P) from 10 to 100. It is clearly found that although the computational cost of the two methods is close for the periodic system with small N_P (below 30), the cost of the global assembly method grows exponentially with N_P. In contrast, the computational consumption of the proposed solution method is kept to be almost constant irrespective of the complexity of the periodic structural system. This clearly implies that the

proposed method would be extremely efficient for dynamic analysis and model-based bolt-loosening detection for large-scale periodic system.

It is also noted that the principal concept of thin-layer element approach is embedded in the proposed dynamic modeling method to simplify the modeling of bolted flange connection. In order to mimic the loosening of bolted-flange connection occurred in the service duration of periodic structural system (e.g., pipeline) in real application, the Young's modulus of the thin-layer material quantifying the connecting stiffness of bolted joint with respect to some pre-specified spans are reduced. This is conveniently accomplished by introducing a nondimensional scalar factor θ_i $(i = 1,2,\dots,10)$ as shown in Fig. 7 to scale the nominal connection stiffness for each individual bolted-flange connection. The initial estimations of these uncertain parameters θ_i are all set to be 1 which indicates the intact status since it is reasonable to assume that the structure is in its healthy condition before one can detect any damage. There are five damage scenarios considered in this paper, and the schematic diagrams and detailed damage configuration are shown in Fig. 10 and Table 2, respectively. By applying a transient bending moment at the left end of the periodic system, the frequency-domain responses are collected from the points located close to each bolted joint, and the first three natural frequencies and mode shapes are identified and utilized for the bolt loosening detection.

As shown in Fig. 11, there are a total number of $N_C = 6$ model classes considered for this periodically supported bolt-connected beam employed in the numerical study. From model classes $\mathcal{C}_1$ to $\mathcal{C}_6$, the parameterization complexity of model class increases with the number of uncertain parameters involved in each class of models. $\mathcal{C}_1$ represents the simplest model class with only one parameter θ_1 to update the connection stiffness of all bolted connections. In model class $\mathcal{C}_2$, the entire periodic structural system is equally separated into two regions, and the connection stiffness of bolted joints within which are quantified by two scalar parameters θ_1 and θ_2, respectively. $\mathcal{C}_3$ and $\mathcal{C}_4$ have the same number of uncertain scaling parameters but different parameterization schemes, which are a little bit more complex than the previous model class $\mathcal{C}_2$. The model class $\mathcal{C}_5$ is presented based on $\mathcal{C}_4$, i.e., the scaling parameter θ_2 in $\mathcal{C}_4$ is further subdivided into two equal regions. $\mathcal{C}_6$ is the model class with the most complex parameterization scheme among all six classes of models, where the bolted connections of the whole periodic structural system are parameterized into five parameter groups each containing two scaling parameters.

Table 3 shows the results of model class selection for each numerical case. The likelihood factors, Ockham factors, logarithm of evidence and the probability of each class of models for each case are obtained using ten sets of modal parameters of the first three modes. It is noted

that the form of logarithm is utilized because the numerical values are extremely large and may induce computational problems. The model class with the highest posterior probability is highlighted in boldface in this table for clarity.

The proposed methodology was firstly confirmed through the utilization of modal measurements obtained from the intact structure. Among the prescribed model classes $\mathcal{C}_j$ $(j = 1,2,\dots,6)$ as shown in Fig. 11, $\mathcal{C}_1$ is selected as the most plausible model class for this periodically supported structural system without bolt loosening. This means that, in healthy case, a sole parameter is enough to capture the vibration characteristics of the complete structural system, and it is not necessary to introduce more complicated parameterization scheme to increase the complexity of the model. In fact, referring to the results of Case 1 listed in Table 3, it is clear that the values of likelihood factors in healthy status of different model classes are very close to each other. This is because each scaling factor in different model classes takes the same nominal value, and all defined model classes fit the data in a similar degree. However, due to the penalty of Ockham factor on the model class complexity, the simplest model class $\mathcal{C}_1$ with the highest evidence is chosen as the most plausible model class for this case.

Different from the healthy scenario, as for the damaged cases, such as Case 2, model class $\mathcal{C}_4$ in this case is selected as the most plausible one among the six candidate model classes. This is understandable as more parameters are needed to depict the stiffness distribution along the structure with the present of local damage. In addition, it is interesting to find that although $\mathcal{C}_2$ is much simpler than $\mathcal{C}_4$, the former is not chosen as the most probable model class. This is due to the fact that the parameter θ_1 of $\mathcal{C}_2$ consists of first five bolted flange joints as shown in Fig. 11, which is ineffective to characterize the actual stiffness reduction occurred only in the 2nd bolted joint as compared with $\mathcal{C}_4$. As a results, the likelihood factor of $\mathcal{C}_2$ tends to be significantly smaller than $\mathcal{C}_4$, even though the former possesses a relatively smaller Ockham factor, making the probability of the latter model class to be larger. Furthermore, comparing $\mathcal{C}_4$ with $\mathcal{C}_6$ for this case, $\mathcal{C}_6$ obviously has a better fit to the data since it has more uncertain model parameters to decrease the discrepancy between the measured and model-predicted modal parameters. Thus the likelihood factor of $\mathcal{C}_6$ is clearly found to be higher than $\mathcal{C}_4$ (63.64 for $\mathcal{C}_4$ and 84.03 for $\mathcal{C}_6$). However, the complexity of $\mathcal{C}_6$ induces more severe penalty from Ockham factor, making $\mathcal{C}_4$ to be chosen as the most plausible model class for this case. On the other hand, it is also noted that the probability of $\mathcal{C}_6$ (44.55%) is actually very close to that of $\mathcal{C}_4$ (48.26%), which indicates the complicated model class having better fit to data is also very competitive sometimes. The results of other cases presented in Table 3 give the similar conclusion as the first two cases, and it is very clear that the combination of

these two factors provides an efficiency way to make a trade-off between the data-fit and parameterization complexity with respect to a model class.

In the second phase of the propose methodology, based on the most plausible model class chosen in the previous stage, the particle filter-based approach is utilized to identify the damaged bolted connection with respect to each damaged case as shown in Table 2. The prior distribution of particles is assumed as uniform priors, and there are 50 particles employed in this approach. The standard deviation of each component in the noise vector $\mathbf{u}^{(k)}$ is assumed as 1% of the range of prior values, and the standard deviation of each element of the noise vector $\mathbf{v}^{(k)}$ is set to be 5% of the measured data. It is noted that the control parameter settings of particle filter-based approach for every model class are identical to keep the consistency for comparison. The particle filter identified results for some selected damage cases, i.e., Case 2 and Case 5, are shown in Figs. 12 and 13 for demonstration, respectively, where only three kinds of model classes are presented for comparison, i.e., the chosen most probable model class, the model classes with the simplest and most complex parameterization schemes. In addition, the statistic properties of identified results for Cases 2 and 5 are summarized in Table 4, where the uncertain parameters containing the actually damaged bolted connections are highlighted in boldface. It is worth mentioning that the identified value of θ_i does not represent the exact connection stiffness of the actually damaged bolted joint, since the number of bolted connections contained in each element group is larger than the number of actually damaged bolt connection for a specified model class.

Take Case 2 as an example, it is clear from Fig. 12 that the uncertain scaling parameters will eventually converge to some constant values, indicating the identified results, after a few number of iterative estimations. Model class with few parameters like $\mathcal{C}_1$ and $\mathcal{C}_2$ can only provide very limited information about the bolt connection failure. For instance, $\mathcal{C}_1$ may only be used to judge whether the structure is damaged or not while $\mathcal{C}_2$ can only identify if the damaged bolted joint is located within the left or right half of the entire periodic system. In contrast, model class with more complex parameterization scheme just like $\mathcal{C}_6$ can provide more accurate and specific information for the damaged bolted joint. However, since the model class $\mathcal{C}_6$ has more uncertain parameters which are needed to be determined, it has a much larger parameter space with higher dimension, and there are more iterative steps required to achieve convergence with the same algorithm settings for the particle filter-based approach. It can be seen in Fig. 12 (f) that it takes more number of interactive steps for θ_3 in $\mathcal{C}_6$ to approach to convergence, implying complex model class generally consumes relatively more computational amount than its simpler counterparts.

In another aspect, the statistical characteristics, i.e., posterior mean value and standard deviation, of identified scaling parameters with respect to all model classes for Case 2 are listed in Table 4. It can be seen that the identified scaling parameters of the most plausible model class $\mathcal{C}_4$ has a relatively smaller value of standard deviation than other model classes in the same case, which clearly indicates that the damage status of bolted-joint groups can be quantified with less uncertainty based on the chosen optimal model class by following the proposed two-phase procedure for detecting the bolted joint loosening. As for other damage cases, such as Case 5, the similar phenomenon can be observed from the corresponding results presented in both Fig. 13 and Table 4. This clearly demonstrates the validity of the proposed methodology.

4. EXPERIMENTAL VERIFICATION

In order to further verify the proposed methodology, in this section, a laboratory model of periodically-supported bolt-connected aluminum beam of length 3m is employed for demonstration. As shown in Fig. 14(a), the periodic beam model consists of five equal spans each with a bolted flange joint in the midspan, and the whole beam model has six supports, which are fixed to the channel steel base by using four M8 steel bolts. The beam segment with length 0.6m between two adjacent supports is considered as the periodic cell, and it's assumed that the cell numbering starts from 1 (leftmost span) to 5 (rightmost span), i.e., the total number of cells in this periodic systems $N_P = 5$. The Young's modulus, mass density, and cross-sectional dimension of the periodic beam model are: 6.89×10^{10} N/m^2, 2.73×10^{10} kg/m^3, and 0.015m×0.045m, respectively. The detail configuration of the bolted flange joint in each midspan is shown in Fig. 14(b), where four M10 steel bolts are utilized. The entire laboratory beam is connected by six beam components with two types, where type I is utilized at the two ends of the periodic structure, and the connection sequence is (type I)-4×(type II)-(type I). The dimensions of these two types of beam components are given in Fig. 15.

Damage to the periodic beam model is introduced by loosening partial bolts in some specified bolted flange joints by using a torque wrench. There are three cases considered for this laboratory beam model as shown in Fig. 16. Case 1 is an intact case, where all the bolts are tightened. Case 2 is a single-damage case, and only the upper two bolts of the bolted flange joints within the 3rd span are loosened. Case 3 is intended to investigate a more difficult damage configuration, where the upper two bolts in the bolted flange joints of the 1st span are further loosened based on the same damage configuration in the previous case. There are five uncertain stiffness scaling parameters $\delta\boldsymbol{\theta} = \{\delta\theta_1, \delta\theta_2, \cdots, \delta\theta_5\}^{\mathrm{T}}$, representing the Young's modulus of thin-layer elements with respect to the connection status for each bolted flange

joint in the proposed dynamic modeling approach, to be identified from experimental modal parameters in both intact and damaged situations.

The experimental configuration for the periodically-supported beam is illustrated in Fig. 17(a). The impact hammer, as shown in Fig. 17(b), is used to excite the periodic beam in direction perpendicular to the beam axis in the vertical plane. The free vibration responses are acquired by five accelerometers (seeing Fig. 17(c)) with sensitivities around 100mV/g attached to the locations close to each joint, and then collected by MPS-140801 signal conditioning box with data acquisition software shown in Figs. 17(d) and (e). A series of repeated free vibration testing are carried out for the laboratory periodic beam model under both healthy and damaged conditions, where the ERA method is employed for modal parameter identification. The sampling frequency is set to be 500 Hz, and the measured duration for each data set is about 10 sec.

The mean values of the first four natural frequencies identified for the laboratory model are shown in Table 5, where the predicted results from the proposed dynamic modeling approach in intact status are also provided. It is clear that model-predicted natural frequencies match well with the measured quantities. Fig. 18 shows the comparison of mode shapes, and it is also obvious that the first four mode shapes calculated from the present analytical model show a good matching with their experimental counterparts. The matching of modal parameters demonstrates the validity of the dynamic modeling approach developed for the bolted flange connection in this paper.

There are five classes of models considered in the experimental verification of the proposed damage identification methodology as shown in Fig. 19. From model classes $\mathcal{C}_1$ to $\mathcal{C}_5$, the complexity of model parameterization increases gradually. Specifically, $\mathcal{C}_1$ with one single parameter θ_1 to scale the connection stiffness of all five bolted flange joints has the lowest degree of complexity among all considered model classes. $\mathcal{C}_2$ is a little bit more complex than $\mathcal{C}_1$, and it has two separated parameters θ_1 and θ_2 to scale the connection stiffness of the first three bolted joints and the rest two, respectively. The number of scaling parameters of $\mathcal{C}_3$ is the same as $\mathcal{C}_2$ but with different parameterization scheme. $\mathcal{C}_4$ has three scaling parameters to update the connection stiffness of the first two, middle and last two bolted joints separately. $\mathcal{C}_5$ is the class of models with the most complex parameterization scheme among all considered model classes, and there are five individual parameters in this class of models to scale each connection stiffness separately.

Table 6 shows the results of model class selection for all model classes with respect to three experimental cases by utilizing the first three sets of modal parameters with five sets of

repeated measurements, and the results corresponding to the identified most probable model class are also highlighted in boldface. As for Case 1, it's clearly found that the most plausible model class is $\mathcal{C}_1$ with the posterior probability of over 99%, possessing the most simple parameterization scheme. This implies that only one parameter is enough for updating the dynamic model of periodic beam with related measurement data in healthy status, which is also consistent with the results obtained in numerical case studies. For Case 2, it is obvious that although the most probable model class is $\mathcal{C}_3$, the posterior probabilities of model classes $\mathcal{C}_2$ and $\mathcal{C}_3$ are actually very competitive (i.e., $p(\mathcal{C}_2|\mathcal{D}) = 33.14\%$ and $p(\mathcal{C}_3|\mathcal{D}) = 34.84\%$). This is not surprised since the damaged bolted joint in this case is expected to have almost the same influence on model classes $\mathcal{C}_2$ and $\mathcal{C}_3$ when referring to the definition of model class as illustrated in Fig. 19. As for Case 3, $\mathcal{C}_2$ is identified as the most probable model class. Different from its competitor $\mathcal{C}_3$, $\mathcal{C}_2$ is able to locate the two damaged bolted connections by using a single parameter θ_1 for this double-damage case, and it is simple enough in this respect. In addition, it is also interesting to note that model class $\mathcal{C}_5$ with the highest likelihood factor is not chosen as the most plausible model class for either damage case due to its relatively higher complexity panelized by the corresponding Ockham factor.

In the second phase of the proposed methodology, the measured modal parameters including both the natural frequencies and mode shapes for the first three modes in damaged cases are employed by the particle filter-based approach to detect the loosening of bolted connection. The scaling parameters are assumed to be uniformly distributed within the predefined domain, and the control parameters for particle filter-based algorithm are the same as the numerical case studies. The history of iterative simultaneous estimation of all scaling parameters given by particle filter-based approach is shown in Fig. 20 for the most probable model classes in Case 2 and Case 3, and the corresponding posterior mean and standard deviation of identified scaling parameter values for each model class are listed in Table 7.

It can be seen from the iteration history that the convergence of the proposed approach is very speedy, and the obtained scaling parameters based on the most plausible model classes clearly pinpoint the actually damaged groups of bolted joints for each case. By comparing the stable solutions for the two cases, it is found that although the scaling parameters θ_2 of the most plausible model class $\mathcal{C}_3$ in Case 2 and θ_1 of $\mathcal{C}_2$ in Case 3 have the similar complexity of parameterization scheme, i.e., they both include three bolted flange joints, the value of θ_2 in the former case is obviously smaller than that of θ_1 in the latter one. Referring to the damage configuration as well as the model class definition provided in Figs. 18 and 19, this phenomenon is well anticipated since the 2nd scaling parameter θ_2 of $\mathcal{C}_3$ includes only a single damaged bolted connection as for Case 2, while the first parameter θ_1 of $\mathcal{C}_2$ contains

two damaged bolted joints in the double-damage case, i.e., Case 3, resulting in a relatively obvious drop of θ_1 of $\mathcal{C}_2$ for this case.

In addition, it can also be found from Table 7 that, the unknown scaling parameters identified from the most probable model class $\mathcal{C}_3$ chosen for Case 2 has a relatively smaller standard deviations than other class of models in the same case. This clearly implies that, besides of pinpointing the damage location and also providing reasonable estimation for damage extent, the scaling parameters indicating the damage status of the corresponding bolted-joint groups can be identified with less uncertainty based on the chosen optimal model class by following the proposed two-phase damage identification methodology.

5. CONCLUSIONS

This paper presented a probabilistic methodology for the detection of bolt loosening on a periodically supported beam-type structural system representing typical industrial pipeline utilizing measured modal parameters. The dynamic model of entire periodic system endowed with bolted flange joints is first developed by utilizing the spectral element method together with the transfer matrix-based approach. A two-staged model-based methodology is then developed to identify the statistic characteristics of uncertain parameters based on the most plausible class of models chosen with suitable parameterization complexity. A comprehensive set of numerical and experimental case studies are performed for demonstration of the validity and efficiency of the proposed methodology.

The obtained results are very encouraging showing that the proposed methodology can efficiently model the dynamic properties of entire periodic system and correctly identify the scaling parameters and associated uncertainties for characterizing the status of bolted connection loosening. Specifically, from the achieved results, it is clearly found that the computational cost for the dynamic analysis of complete periodic systems based on the proposed model is almost constant irrespective of the number of cells contained, showing the significant efficiency for model-based damage detection of large-scale periodic system with a huge amount of repeated units. In addition, it is also shown that the combination of likelihood and Ockham factors provides a mathematically rigorous and efficient way to pinpoint the most probable class of models with an appropriate degree of parameterization complexity for the purpose of structural damage detection. Furthermore, it is also seen from the results of both numerical and experimental case studies that, the stiffness scaling parameters identified from the most probable class of models possess a relatively lower level of uncertainty and rapid convergence capability as compared to its competitive counterparts, which is essential for the fast diagnose of the failure of large-scale periodic structural system in real application. It

should be also pointed that, the proposed shear-resistant parameter of the thin-layer element is kept to be some tiny value in the present case studies, as there is no trend of relative shear deformation or slip occurred between the two opposite flange surface with respect to the first few modes involved for bolt loosening detection. Also, it is noted that the results of model class selection depend on many other factors, such as the sensor configuration, and utilized modal information, etc., which will be further investigated and reported in subsequent technique publications.

ACKNOWLEDGMENTS

The authors gratefully acknowledge the financial support provided by the National Natural Science Foundation of China (Grants No. 51778506, 51838006, and 51578260), and a scholarship from the China Scholarship Council (File No. 201806275091) while the first author visiting the Center for Engineering Dynamics and Institute for Risk and Uncertainty in the University of Liverpool. The authors would also like to thank the Editor and the anonymous reviewers for their constructive comments and valuable suggestions to improve the quality of the article.

APPENDIX A

In Eq. (10), the DSM with sub-cell number $e = 1, \cdots, 5, 7, 8, 10$ takes the same form as that given in [49], and the partitioned matrices of DSM in this paper can be further rewritten as, respectively,

$$\begin{aligned}
\mathbf{D}_{LL,n}^{(e)} &= \begin{bmatrix} \eta\cos k_r L & 0 & 0 \\ 0 & \alpha EI/L^3 & \bar{\gamma} EI/L^2 \\ 0 & \bar{\gamma} EI/L^2 & \beta EI/L \end{bmatrix} \\
\mathbf{D}_{LR,n}^{(e)} &= \begin{bmatrix} -\eta & 0 & 0 \\ 0 & -\bar{\alpha} EI/L^3 & \gamma EI/L^2 \\ 0 & -\gamma EI/L^2 & \bar{\beta} EI/L \end{bmatrix} \\
\mathbf{D}_{RL,n}^{(e)} &= \begin{bmatrix} -\eta & 0 & 0 \\ 0 & -\bar{\alpha} EI/L^3 & -\gamma EI/L^2 \\ 0 & \gamma EI/L^2 & \bar{\beta} EI/L \end{bmatrix} \\
\mathbf{D}_{RR,n}^{(e)} &= \begin{bmatrix} \eta\cos k_r L & 0 & 0 \\ 0 & \alpha EI/L^3 & -\bar{\gamma} EI/L^2 \\ 0 & -\bar{\gamma} EI/L^2 & \beta EI/L \end{bmatrix}
\end{aligned} \tag{A1}$$

where

$$
\begin{aligned}
\alpha &= (\cos k_b L \sinh k_b L + \sin k_b L \cosh k_b L)(k_b L)^3/\delta \\
\bar{\alpha} &= (\sin k_b L + \sinh k_b L)(k_b L)^3/\delta \\
\beta &= (-\cos k_b L \sinh k_b L + \sin k_b L \cosh k_b L) k_b L/\delta \\
\bar{\beta} &= (-\sin k_b L + \sinh k_b L) k_b L/\delta \\
\gamma &= (-\cos k_b L + \cosh k_b L)(k_b L)^2/\delta \\
\bar{\gamma} &= \sin k_b L \sinh k_b L (k_b L)^2/\delta \\
\delta &= 1 - \cos k_b L \cosh k_b L \\
\eta &= EA k_r/(\sin k_r L)
\end{aligned}
\tag{A2}
$$

and the two wavenumbers k_b and k_r are given by, respectively,

$$
k_b = \left(\frac{\omega^2 \rho A}{EI}\right)^{\frac{1}{4}}, \quad k_r = \left(-\frac{\omega^2 \rho A}{EA}\right)^{\frac{1}{2}} \tag{A3}
$$

It should be noted that the DSM $\mathbf{D}_n^{(e)}$ for each sub-cell shown in Eq. (A1) depends on the geometric and material properties of specified sub-cell with number e even though it is not explicitly reflected in the corresponding variable symbols in this equation for simplicity.

APPENDIX B

For sub-cell 6 shown in Fig. 3, it is assumed that the thin-layer element is separated into two equal-thickness sublayers by a shear spring located at the middle along the thickness direction of thin layer, and there thus exists a hypothetical boundary at the location of shear spring. Defining two local axial coordinate systems for the two separated sublayers, the corresponding two coordinate origins are located at the left end of each sublayer. By following the Euler-Bernoulli beam theory, the transverse displacements of the two sub-layers at frequency ω_n can be expressed as ($0 \le x \le T_c,\ T_c = T_L/2$), respectively,

$$
w_{L,n}^{(6)}(x) = \mathbf{N}_{L,n}^{(6)}(x)\mathbf{G}_L^{(6)}, \quad w_{R,n}^{(6)}(x) = \mathbf{N}_{R,n}^{(6)}(x)\mathbf{G}_R^{(6)} \tag{B1}
$$

where the subscripts L and R denote the left and right parts of the thin-layer element. $w_{L,n}^{(6)}(x)$ and $w_{R,n}^{(6)}(x)$ are the transverse displacements at the two sub-layer elements, respectively, and

$$
\begin{aligned}
\mathbf{N}_{L,n}^{(6)}(x) &= \{\sin k_b x \ \cos k_b x \ \sinh k_b x \ \cosh k_b x\} \\
\mathbf{N}_{R,n}^{(6)}(x) &= \{\sin k_b (x + T_c) \ \cos k_b (x + T_c) \ \sinh k_b (x + T_c) \ \cosh k_b (x + T_c)\}
\end{aligned}
\tag{B2}
$$

The unknown coefficients $\mathbf{G}_L^{(6)} = \{G_1\ G_2\ G_3\ G_4\}^{\mathrm{T}}$ and $\mathbf{G}_R^{(6)} = \{G_5\ G_6\ G_7\ G_8\}^{\mathrm{T}}$ in Eq. (B1) are to be identified by both the continuity and boundary conditions.

Considering the left and right boundary conditions at the two ends of the thin-layer element, one can get that

$$w_{L,n}^{(6)}(x)\Big|_{x=0} = w_{14,n},\ \ \partial w_{L,n}^{(6)}(x)/\partial x\Big|_{x=0} = \phi_{14,n} \tag{B3}$$

$$w_{R,n}^{(6)}(x)\Big|_{x=T_c} = w_{15,n},\ \ \partial w_{R,n}^{(6)}(x)/\partial x\Big|_{x=T_c} = \phi_{15,n} \tag{B4}$$

The continuous condition at the hypothetical boundary are given by

$$w_{L,n}^{(6)}(x)\Big|_{x=T_c} - w_{R,n}^{(6)}(x)\Big|_{x=0} = \Theta\partial^3 w_{L,n}^{(6)}(x)/\,\partial x^3\Big|_{x=T_c} \tag{B5}$$

$$\partial w_{L,n}^{(6)}(x)/\,\partial x\Big|_{x=T_c} = \partial w_{R,n}^{(6)}(x)/\,\partial x\Big|_{x=0} \tag{B6}$$

$$\partial^2 w_{L,n}^{(6)}(x)/\,\partial x^2\Big|_{x=T_c} = \partial^2 w_{R,n}^{(6)}(x)/\,\partial x^2\Big|_{x=0} \tag{B7}$$

$$\partial^3 w_{L,n}^{(6)}(x)/\,\partial x^3\Big|_{x=T_c} = \partial^3 w_{R,n}^{(6)}(x)/\,\partial x^3\Big|_{x=0} \tag{B8}$$

where the parameter Θ is introduced to characterize the shear-resistant capability of the thin-layer element.

By substituting Eqs. (B1) and (B2) into both the boundary and continuity conditions given in Eqs. (B3) to (B8), a set of homogeneous equations can be obtained as

$$\begin{bmatrix}
ak_b & -bk_b & ck_b & dk_b & -ak_b & bk_b & -ck_b & -dk_b \\
-b+\Theta a{k_b}^3 & -a-\Theta b{k_b}^3 & -d-\Theta c{k_b}^3 & -c-\Theta d{k_b}^3 & b & a & d & c \\
0 & 1 & 0 & 1 & 0 & 0 & 0 & 0 \\
k_b & 0 & k_b & 0 & 0 & 0 & 0 & 0 \\
-b{k_b}^2 & -a{k_b}^2 & d{k_b}^2 & c{k_b}^2 & b{k_b}^2 & a{k_b}^2 & -d{k_b}^2 & -c{k_b}^2 \\
-a{k_b}^3 & b{k_b}^3 & c{k_b}^3 & d{k_b}^3 & a{k_b}^3 & -b{k_b}^3 & -c{k_b}^3 & -d{k_b}^3 \\
0 & 0 & 0 & 0 & b_L & a_L & d_L & c_L \\
0 & 0 & 0 & 0 & a_Lk_b & -b_Lk_b & c_Lk_b & d_Lk_b
\end{bmatrix}
\begin{Bmatrix} G_1 \\ G_2 \\ G_3 \\ G_4 \\ G_5 \\ G_6 \\ G_7 \\ G_8 \end{Bmatrix}
=
\begin{Bmatrix} w_{14,n} \\ \phi_{14,n} \\ 0 \\ 0 \\ 0 \\ 0 \\ w_{15,n} \\ \phi_{15,n} \end{Bmatrix} \tag{B9}$$

where

$$a = \cos k_b T_c,\ \ b = \sin k_b T_c,\ \ c = \cosh k_b T_c,\ \ d = \sinh k_b T_c$$

$$a_L = \cos k_b T_L,\ b_L = \sin k_b T_L,\ c_L = \cosh k_b T_L,\ d_L = \sinh k_b T_L$$

On the other hand, the bending moment and shear forces at two ends of the thin-layer element can be expressed, respectively, as

$$M_{14,n} = -EI\partial^2 w_{L,n}^{(6)}(x)/\partial x^2\Big|_{x=0},\ V_{14,n} = EI\partial^3 w_{L,n}^{(6)}(x)/\partial x^3\Big|_{x=0} \tag{B10}$$

$$M_{15,n} = EI\partial^2 w_{R,n}^{(6)}(x)/\partial x^2\Big|_{x=T_c},\ V_{15,n} = -EI\partial^3 w_{R,n}^{(6)}(x)/\partial x^3\Big|_{x=T_c} \tag{B11}$$

Similarly, substitute Eqs. (B1) and (B2) into Eqs. (B10) and (B11), the following set of homogeneous equations can be obtained,

$$EI\begin{bmatrix} -k_b{}^3 & 0 & k_b{}^3 & 0 & & \mathbf{0} & & \\ 0 & k_b{}^2 & 0 & -k_b{}^2 & & & & \\ & & & & a_L k_b{}^3 & -b_L k_b{}^3 & -c_L k_b{}^3 & -d_L k_b{}^3 \\ & \mathbf{0} & & & -b_L k_b{}^2 & -a_L k_b{}^2 & d_L k_b{}^2 & c_L k_b{}^2 \end{bmatrix}\begin{Bmatrix} G_1 \\ G_2 \\ G_3 \\ G_4 \\ G_5 \\ G_6 \\ G_7 \\ G_8 \end{Bmatrix} = \begin{Bmatrix} V_{14,n} \\ M_{14,n} \\ V_{15,n} \\ M_{15,n} \end{Bmatrix} \tag{B12}$$

By combining Eqs. (B9) and (B12) and eliminating the unknown coefficients G_1 to G_8, the following dynamic equilibrium equation for sub-cell 6 can be obtained as below:

$$EI\begin{bmatrix} k_{11} & k_{12} & k_{13} & k_{14} \\ k_{21} & k_{22} & k_{23} & k_{24} \\ k_{31} & k_{32} & k_{33} & k_{34} \\ k_{41} & k_{42} & k_{43} & k_{44} \end{bmatrix}\begin{Bmatrix} w_{14,n} \\ \phi_{14,n} \\ w_{15,n} \\ \phi_{15,n} \end{Bmatrix} = \begin{Bmatrix} V_{14,n} \\ M_{14,n} \\ V_{15,n} \\ M_{15,n} \end{Bmatrix} \tag{B13}$$

where

$$k_{11} = -k_b{}^3\left[4a_L d_L + 4c_L b_L + \Theta k_b{}^3(c_L - a_L + 2b_L d_L + 4bd)\right]/2/\Delta$$

$$k_{12} = -\left[4k_b{}^2 b_L d_L + \Theta k_b{}^5(c_L b_L - a_L d_L - 2ad + 2cb)\right]/\Delta$$

$$k_{13} = k_b{}^3\left[4b_L + 4d_L + \Theta k_b{}^3(c_L - a_L - 4bd)\right]/2/\Delta$$

$$k_{14} = k_b{}^2\left[(a+c)\left(4a - 4c + \Theta k_b{}^3(b-d)\right)\right]/\Delta$$

$$k_{22} = k_b\left[4a_L d_L - 4c_L b_L + \Theta k_b{}^3(c_L + a_L + 2a_L c_L + 4ac)\right]/2/\Delta$$

$$k_{24} = -k_b\left(2d_L - 2b_L + \Theta k_b{}^3(a+c)^2\right)/\Delta$$

$$k_{21} = k_{12},\ k_{23} = -k_{14},\ k_{31} = k_{13},\ k_{32} = k_{23},\ k_{33} = k_{11}$$

$$k_{34} = -k_{12},\ k_{41} = k_{14},\ k_{42} = k_{24},\ k_{43} = k_{34},\ k_{44} = k_{22}$$

$$\Delta = 2(2a^2 - 1)(2c^2 - 1) - 2 + \Theta {k_b}^3 (a^2 d_L + c^2 b_L + 2ad + 2cb)$$

To be consistent with the matrix dimension, Eq. (B13) can be further expanded by including the effects of longitudinal displacement and corresponding axial force form as

$$\begin{bmatrix} \mathbf{D}_{LL,n}^{(6)} & \mathbf{D}_{LR,n}^{(6)} \\ \mathbf{D}_{RL,n}^{(6)} & \mathbf{D}_{RR,n}^{(6)} \end{bmatrix} \begin{Bmatrix} \mathbf{U}_{14,n} \\ \mathbf{U}_{15,n} \end{Bmatrix} = \begin{Bmatrix} \mathbf{F}_{14,n} \\ \mathbf{F}_{15,n} \end{Bmatrix} \tag{B14}$$

where $\mathbf{U}_{m,n} = \{u_{m,n}\ w_{m,n}\ \phi_{m,n}\}^{\mathrm{T}}$, and $\mathbf{F}_{m,n} = \{N_{m,n}\ V_{m,n}\ M_{m,n}\}^{\mathrm{T}}$ $(m = 14 \text{ or } 15)$. With Eq. (B14), the DSM of the sub-cell 6 representing the thin-layer element is obtained, and the DSM of sub-cell 9 can be obtained in a similar way, which is utilized in Eq. (22).

REFERENCES

[1] M. Maldovan, Sound and heat revolutions in phononics, Nature 503 (2013) 209–217.

[2] L. Brillouin, Wave propagation in periodic structures, Dover Publications Inc., New York, 1964.

[3] D.J. Mead, Wave propagation in continuous periodic structures: research contributions from Southampton 1964–1995, J. Sound Vib. 190 (1996) 495–524.

[4] D. Yu, J. Wen, H. Zhao, Y. Liu, X. Wen. Vibration reduction by using the idea of phononic crystals in a pipe-conveying fluid, J. Sound Vib. 318 (2008) 193–205.

[5] Q.X. Fu, J.F. Lu, A model for the wave localization in a disordered periodic elevated railway undergoing in-plane vibration, J. Vib. Acoust. 135 (2013) 521–523.

[6] H.F. Lam, Q. Hu, M.T. Wong, The Bayesian methodology for the detection of railway ballast damage under a concrete sleeper, Eng. Struct. 81 (2014) 289–301.

[7] G. Carta, M. Brun, Bloch-Floquet waves in flexural systems with continuous and discrete elements, Mech. Mater. 87 (2015) 11–26.

[8] O.O. Bendiksen, Localization phenomena in structural dynamics, Chaos Soliton. Fract. 11 (2000) 1621–1660.

[9] A. Baz, Active control of periodic structures, J. Vib. Acoust. 123 (2001) 472–479.

[10] L. Ding, H.P. Zhu, T. Yin, Wave propagation in a periodic elastic-piezoelectric axial-bending coupled beam, J. Sound Vib. 332 (2013) 6377–6388.

[11] K. Manktelow, R.K. Narisetti, M.J. Leamy, M. Ruzzene, Finite-element based perturbation analysis of wave propagation in nonlinear periodic structures, Mech. Syst. Signal Pr. 39 (2013) 32–46.

[12] R. Chen, T.X. Wu, Vibration reduction in a periodic truss beam carrying locally resonant oscillators, J. Vib. Control 22 (2014) 1–16.

[13] B. Bao, D. Guyomar, M. Lallart, Vibration reduction for smart periodic structures via periodic piezoelectric arrays with nonlinear interleaved-switched electronic networks, Mech. Syst. Signal Pr. 82 (2017) 230–259.

[14] H.P. Zhu, L. Ding, T. Yin. Wave propagation and localization in a randomly disordered periodic piezoelectric axial-bending coupled beam. Adv. Struct. Eng. 16 (2013) 1513–1522.

[15] K.V. Yuen. Updating large models for mechanical systems using incomplete modal measurement, Mech. Syst. Signal Pr. 28 (2012) 297–308.

[16] K.V. Yuen, S.C. Kuok, Online updating and uncertainty quantification using nonstationary output-only measurement, Mech. Syst. Signal Pr. 66–67 (2016) 62–77.

[17] H. Zhu, M. Wu, The characteristic receptance method for damage detection in large mono-coupled periodic structures, J. Sound Vib. 251 (2002) 241–259.

[18] H.P. Zhu, Y.L. Xu, Damage detection of mono-coupled periodic structures based on sensitivity analysis of modal parameters, J. Sound Vib. 285 (2005) 365–390.

[19] T. Yin, H.P. Zhu, S.J. Fu, Damage identification of periodically-supported structures following the Bayesian probabilistic approach, Int. J. Struct. Stab. Dyn. 19 (2019) 1940011.

[20] E.P. Carden, F. Fanning, Vibration based condition monitoring: A review, Struct. Health Monit. 3 (2004) 355–377.

[21] T. Yin, H.F. Lam, H.M. Chow, H.P. Zhu, Dynamic reduction-based structural damage detection of transmission tower utilizing ambient vibration data, Eng. Struct. 31 (2009) 2009-2019.

[22] T. Yin, H.F. Lam, H.M. Chow, A Bayesian probabilistic approach for crack characterization in plate structures, Comput.-Aided Civ. Infrastruct. Eng. 25 (2010) 375–386.

[23] H.F. Lam, T. Yin, Dynamic reduction-based structural damage detection of transmission towers: Practical issues and experimental verification, Eng. Struct. 33 (2011) 1459–1478.

[24] S.K. Au, F.L. Zhang, Ambient modal identification of a primary–secondary structure by Fast Bayesian FFT method, Mech. Syst. Signal Pr. 28 (2012) 280–296.

[25] H.F. Lam, T. Yin, Application of two-dimensional spatial wavelet transform in the detection of an obstructed crack on a thin plate, Struct. Control Hlth. 19 (2012) 260–277.

[26] T. Yin, H.F. Lam, Dynamic analysis of finite-length circular cylindrical shells with a circumferential surface crack, J. Eng. Mech.-ASCE 139 (2013) 1419–1434.

[27] H. Qarib, H. Adeli, Recent advances in health monitoring of civil structures, Sci. Iran. 21 (2014) 1733–1742.

[28] T. Yin, Q.H. Jiang, K.V. Yuen, Vibration-based damage detection for structural connections using incomplete modal data by Bayesian approach and model reduction technique, Eng. Struct. 132 (2017) 260–277.

[29] Y. Watanabe, N. Sugimoto, Flexural wave propagation in a spatially periodic structure of articulated beams, Wave Motion 42 (2005) 155–167.

[30] T. Yin, K.V. Yuen, H.F. Lam, H.P. Zhu, Entropy-based optimal sensor placement for model identification of periodic structures endowed with bolted joints, Comput.-Aided Civ. Infrastruct. Eng. 32 (2017) 1007–1024.

[31] L. Gaul, J. Lenz, Nonlinear dynamics of structures assembled by bolted joints, Acta Mech. 125 (1997) 169–181.

[32] Y. Luan, Z.Q. Guan, G.D. Cheng, S. Liu, A simplified nonlinear dynamic model for the analysis of pipe structures with bolted flange joints, J. Sound Vib. 331 (2012) 325–344.

[33] J.E. Mottershead, M.I. Friswell, Model updating in structural dynamics: a survey, J. Sound Vib. 162 (1993) 347–375.

[34] M.I. Friswell, J.E. Mottershead, Finite element model updating in structural dynamics, Kluwer Academic Press, Dordrecht, 1995.

[35] C. Mares, J.E. Mottershead, M.I. Friswell. Stochastic model updating: Part 1—theory and simulated example, Mech. Syst. Signal Pr. 20 (2006) 1674–1695.

[36] J.E. Mottershead, C. Mares, S. James, M.I. Friswell, Stochastic model updating: Part 2—application to a set of physical structures, Mech. Syst. Signal Pr. 20 (2006) 2171–2185.

[37] J.E. Mottershead, M. Link, M.I. Friswell, The sensitivity method in finite element model updating: A tutorial, Mech. Syst. Signal Pr. 25 (2011) 2275–2296.

[38] H.F. Lam, J. Hu, J.H. Yang, Bayesian operational modal analysis and Markov chain Monte Carlo-based model updating of a factory building, Eng. Struct. 132 (2017): 314–336.

[39] J.E. Mottershead, W.X. Shao, Correction of joint stiffnesses and constraints for finite element models in structural dynamics, J. Appl. Mech.-T. ASME 60 (1993) 117–122.

[40] J.E. Mottershead, M.I. Friswell, G.H. Ng, J.A. Brandon, Geometric parameters for finite element updating of joints and constraints, Mech. Syst. Signal Pr. 10 (1996) 171–182.

[41] J. Mackerle, Finite element analysis of fastening and joining: A bibliography (1990–2002), Int. J. Pres. Ves. Pip. 80 (2003) 253–271.

[42] S. Bograd, P. Reuss, A. Schmidt, L. Gaul, M. Mayer, Modeling the dynamics of mechanical joints, Mech. Syst. Signal Pr. 25 (2011) 2801–2826.

[43] H. Ahmadian, J.E. Mottershead, S. James, M.I. Friswell, C.A. Reece, Modelling and updating of large surface-to-surface joints in the awe-mace structure, Mech. Syst. Signal Pr. 20 (2006) 868–880.

[44] H. Ahmadian, H. Jalali, Generic element formulation for modelling bolted lap joints, Mech. Syst. Signal Pr. 21 (2007) 2318–2334.

[45] M.H. Mayer, L. Gaul, Segment-to-segment contact elements for modelling joint interfaces in finite element analysis, Mech. Syst. Signal Pr. 21 (2007) 724–734.

[46] C. Desai, M. Zaman, J. Lightner, H. Siriwardane, Thin-layer element for interfaces and joints, Int. J. Numer. Anal. Met. 8 (1984) 19–43.

[47] J.F. Doyle, Wave propagation in structures: spectral analysis using fast discrete Fourier transforms, Springer, New York, 1997.

[48] U. Lee, Spectral element method in structural dynamics, John Wiley & Sons, Singapore, 2009.

[49] J.B. Zhang, Structural dynamic analysis based on spectral element method, PhD Thesis, Huazhong University of Science and Technology, China, 2006.

[50] J.L. Beck, K.V. Yuen, Model selection using response measurement: a Bayesian probabilistic approach, J. Eng. Mech.-ASCE 130 (2004) 192–203.

[51] S.C. Kuok, Yuen, Ka-Veng, Investigation of modal identification and modal identifiability of a cable-stayed bridge with Bayesian framework, Smart Struct. Syst. 17 (2016): 445–470.

[52] J.L. Beck, L.S. Katafygiotis, Updating models and their uncertainties I: Bayesian statistical framework, J. Eng. Mech.-ASCE, 124 (1998) 455–461.

[53] O. Sedehi, C. Papadimitriou, L.S. Katafygiotis, Probabilistic hierarchical Bayesian framework for time-domain model updating and robust predictions, Mech. Syst. Signal Pr. (2018). (In press)

[54] C. Papadimitriou, J.L. Beck, Katafygiotis LS. Asymptotic expansions for reliabilities and moments of uncertain dynamic systems, J. Eng. Mech.-ASCE 123 (1997) 1219–1229.

[55] N.J. Gordon, D.J. Salmond, A.F.M. Smith, Novel approach to nonlinear/non-Gaussian Bayesian state estimation, IEE P. 140 (1993) 107-113.

[56] A. Doucet, S. Godsill, C. Andrieu, On sequential Monte Carlo sampling methods for Bayesian filtering, Stat. Comput. 10 (2000) 197–208.

[57] J. Liu, Metropolized independent sampling with comparisons to rejection sampling and importance sampling, Stat. Comput. 6 (1996) 113–119.

[58] B. Goller, J.L. Beck, G.I. Schu¨ller. Evidence-based identification of weighting factors in Bayesian model updating using modal data, J. Eng. Mech.-ASCE 138 (2012) 430–440.

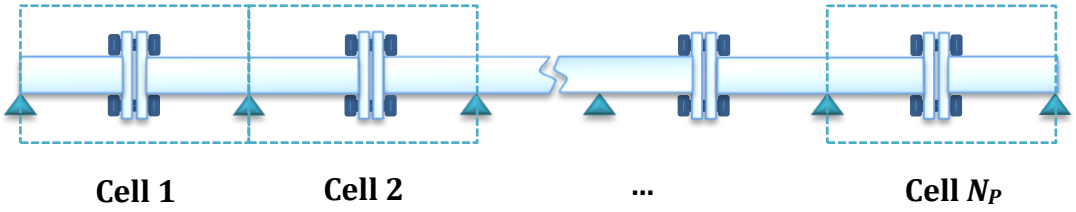

Fig. 1. Schematic of periodically supported beam endowed with bolted flange joints in each midspan.

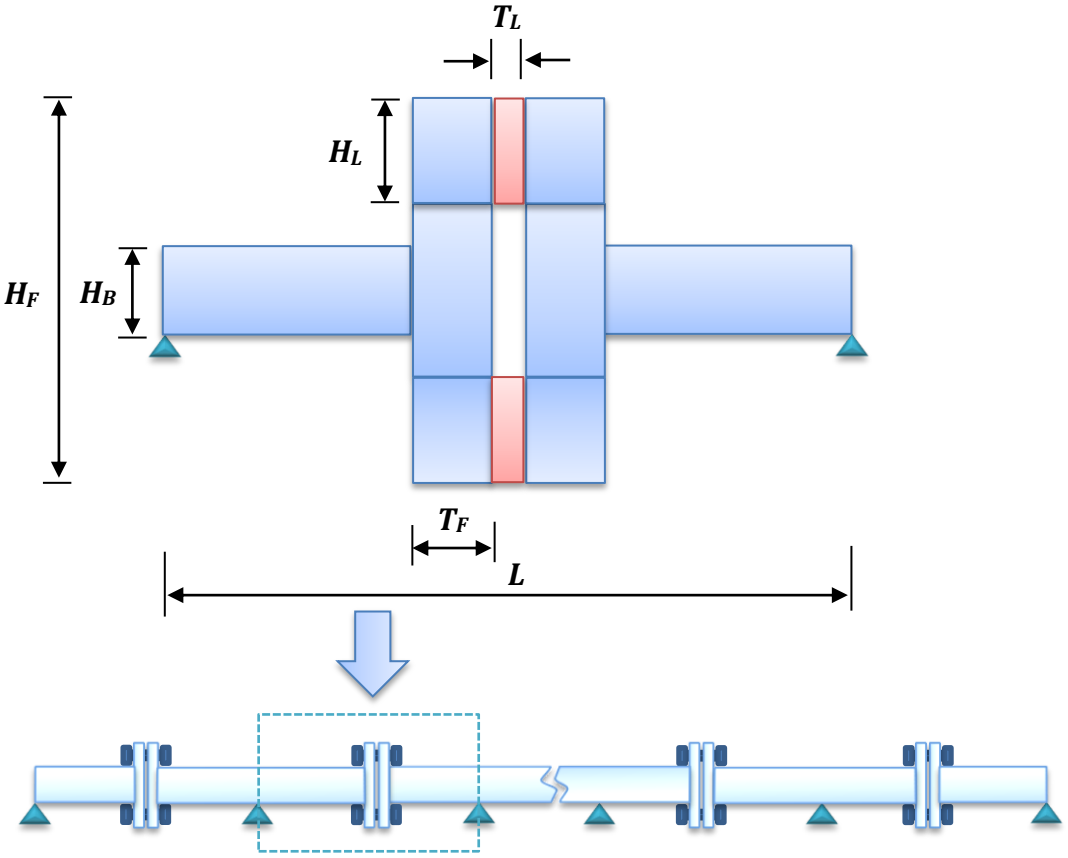

Fig. 2. Discretization scheme of one periodic cell endowed with a bolted flange joint.

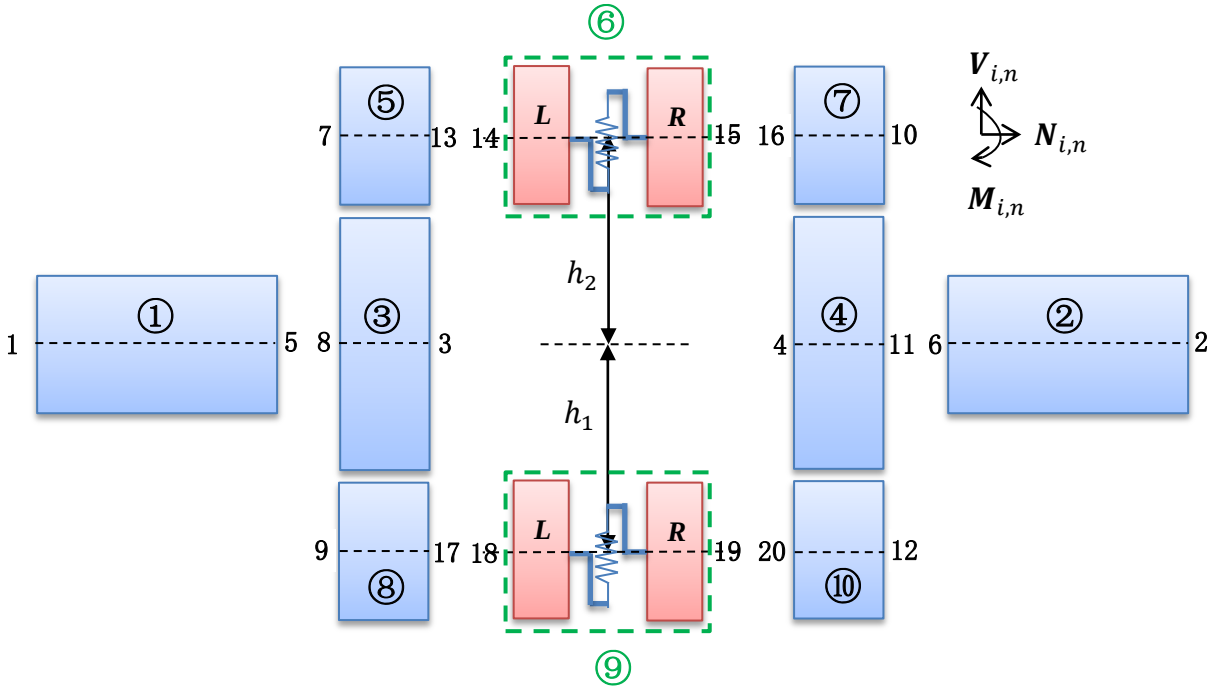

Fig. 3. Discretization model of one cell for spectral element modeling.

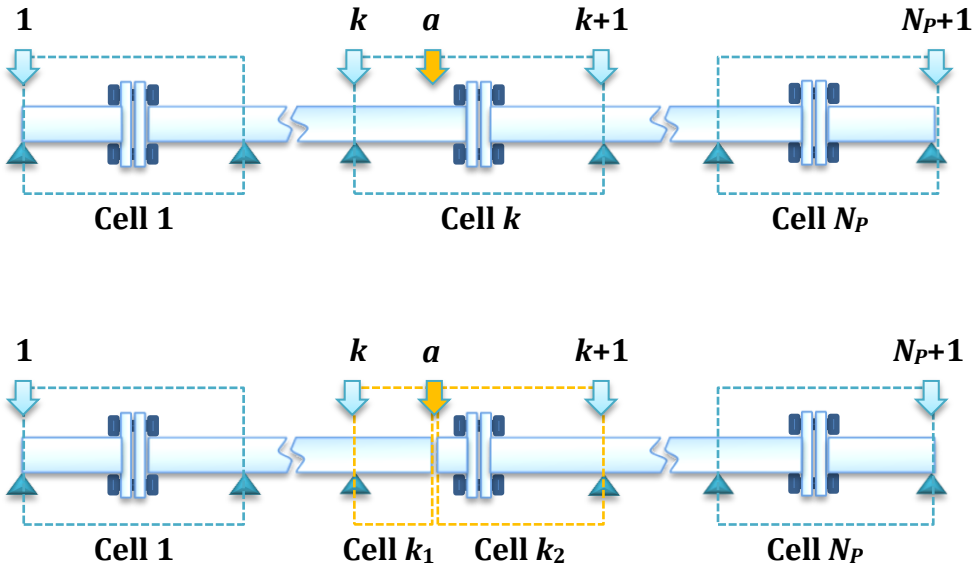

Fig. 4. Subdivision scheme for extracting dynamic response at a given point *a*.

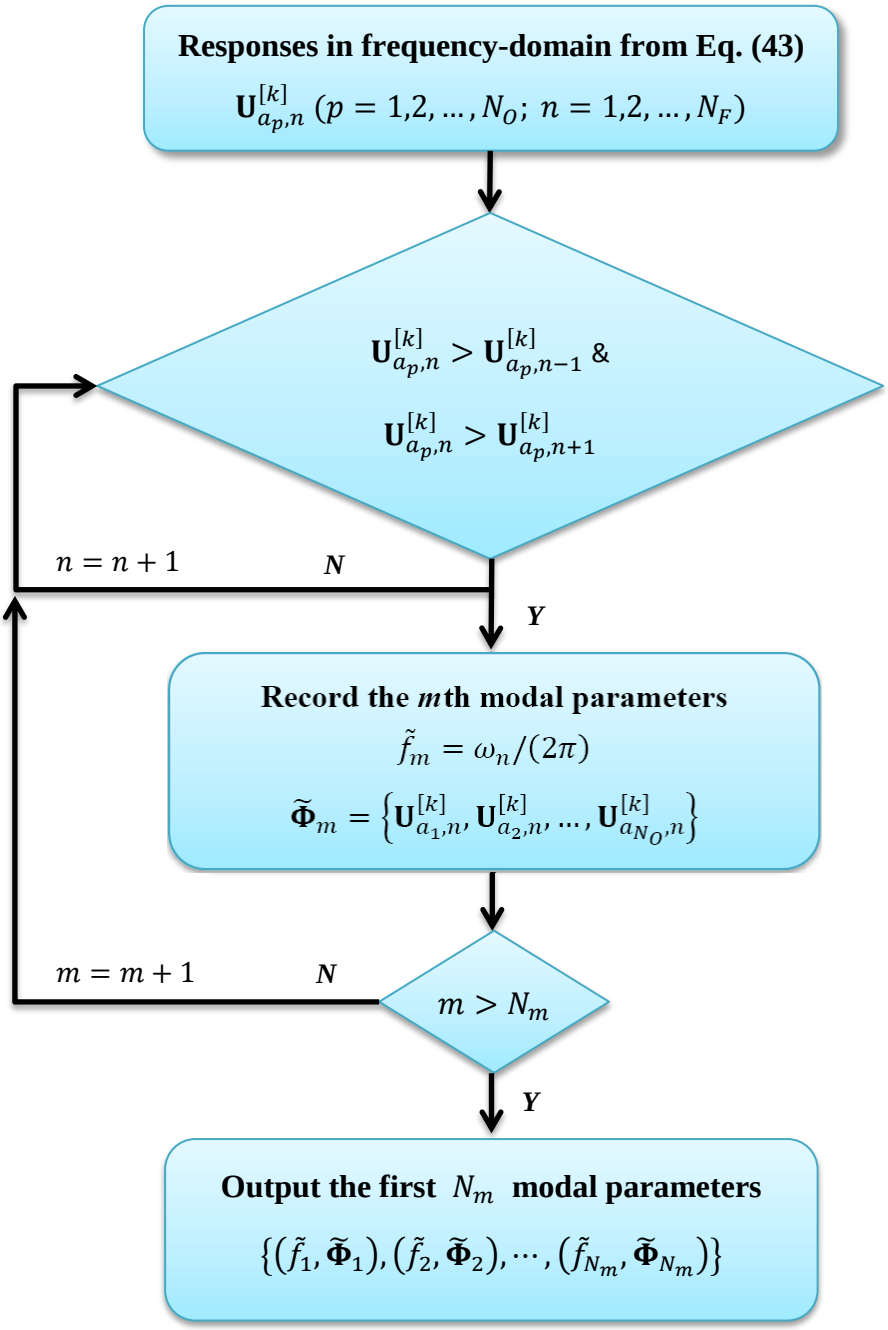

Fig.5. Procedure of calculating natural frequencies and mode shapes from frequency-domain responses.

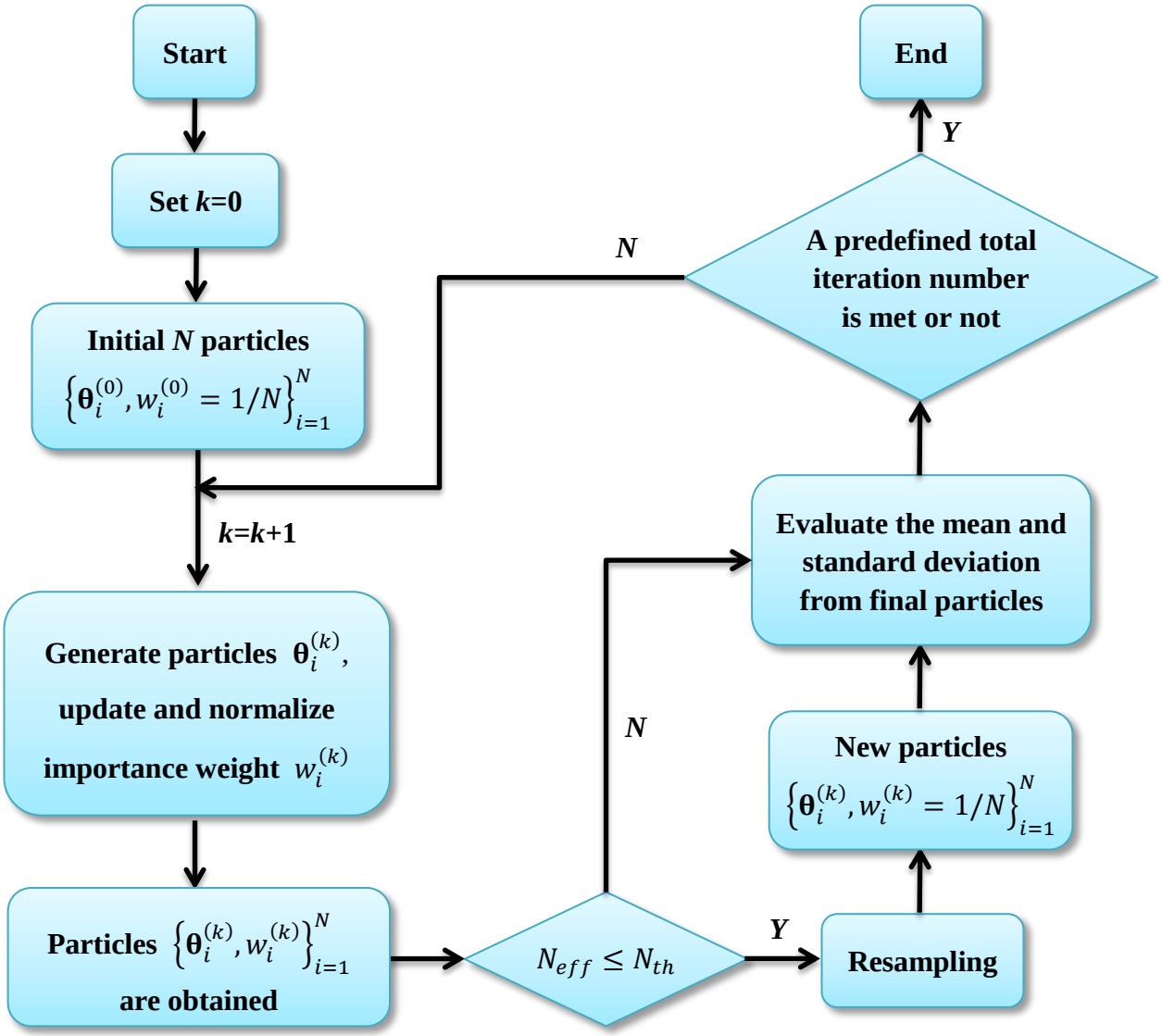

Fig.6. Flowchart of the proposed particle filter-based bolt-loosening identification method.

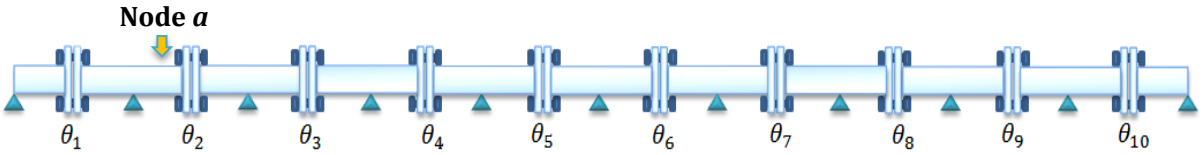

Fig. 7. A ten-span periodically supported beam endowed with bolted flange joints (with arbitrary node *a*).

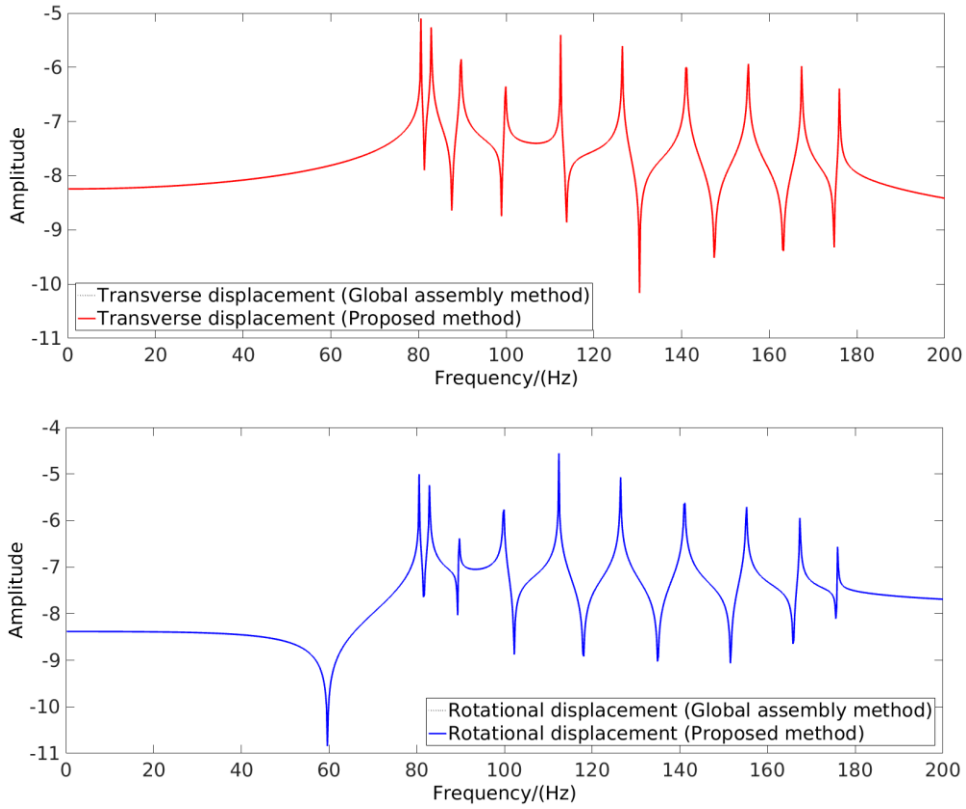

Fig. 8. Frequency-domain transverse and rotational displacements at node *a*: (up) transverse displacements; (bottom) rotational displacements.

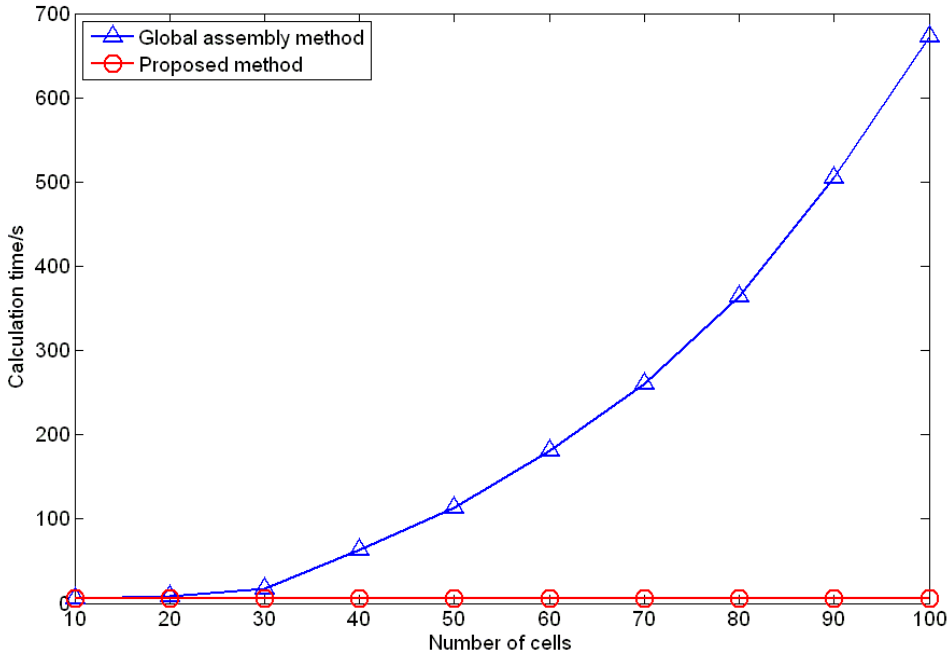

Fig. 9. Time used for calculating transvers response at node *a* by using the global assembly method and the proposed method.

(a) Damage configuration in Case 2

(b) Damage configuration in Case 3

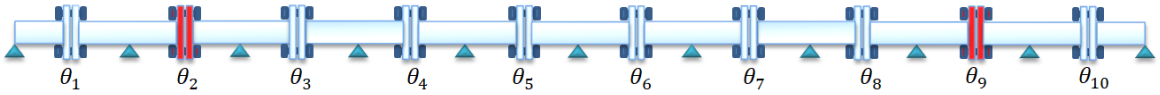

(c) Damage configuration in Case 4

(d) Damage configuration in Case 5

Fig. 10. Damage cases considered for the loosening of bolted joints (damaged joints marked in red).

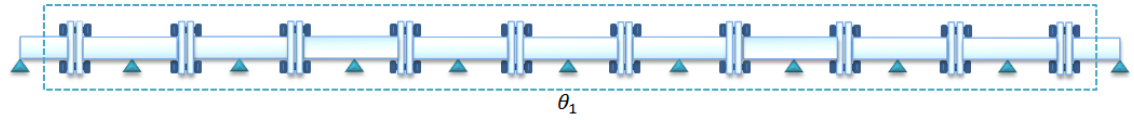

(a) Model class $\mathcal{C}_1$

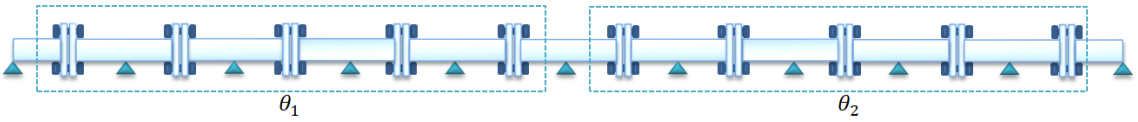

(b) Model class $\mathcal{C}_2$

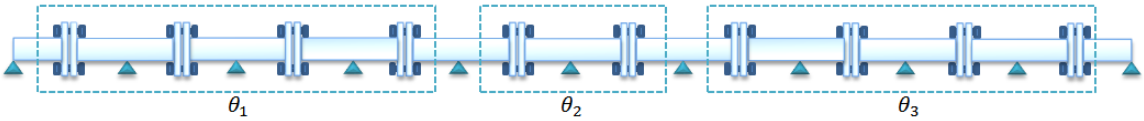

(c) Model class $\mathcal{C}_3$

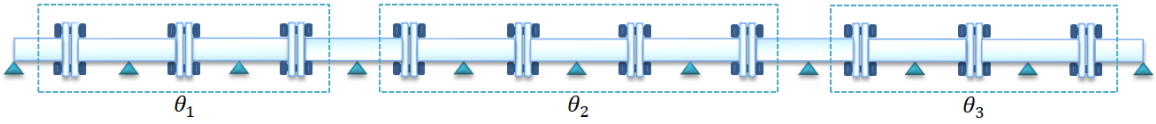

(d) Model class $\mathcal{C}_4$

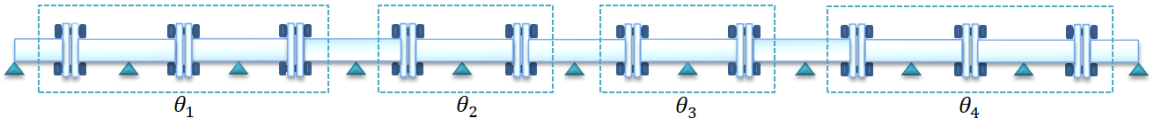

(e) Model class $\mathcal{C}_5$

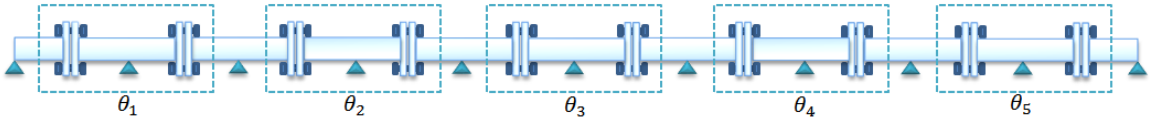

(f) Model class $\mathcal{C}_6$

Fig. 11. Various model classes employed for detection of bolt loosening in the numerical study.

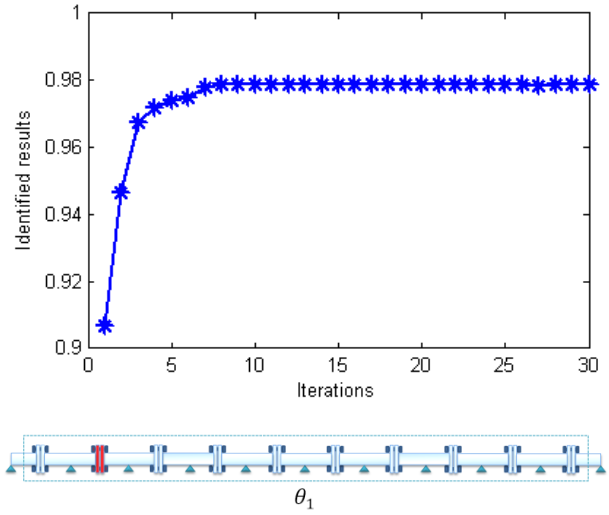

(a) Model class $\mathcal{C}_1$

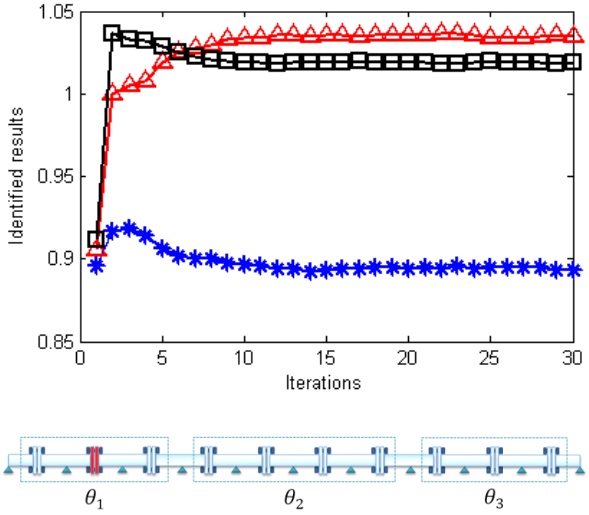

(b) Model class $\mathcal{C}_4$

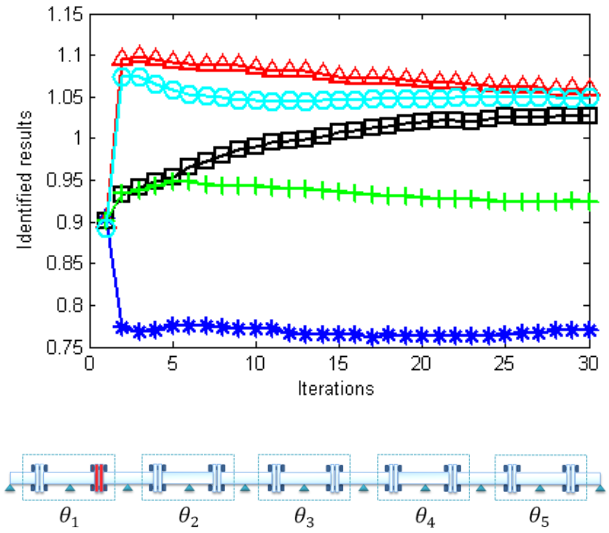

(c) Model class $\mathcal{C}_6$

Fig. 12. History of iterative simultaneous estimation by the particle filter-based approach for Case 2 in the numerical study.

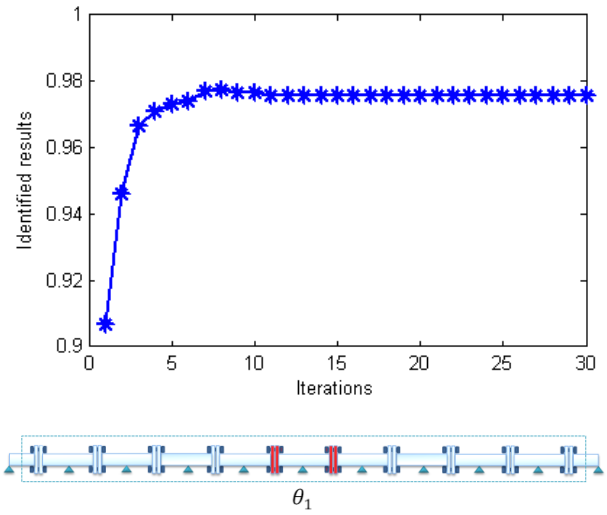

(a) Model class $\mathcal{C}_1$

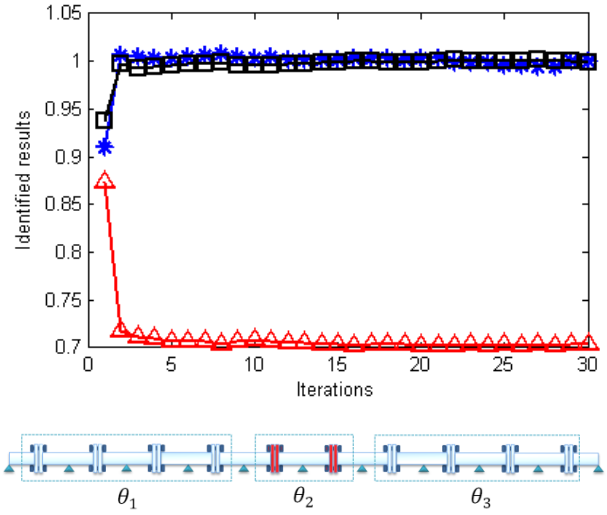

(b) Model class $\mathcal{C}_3$

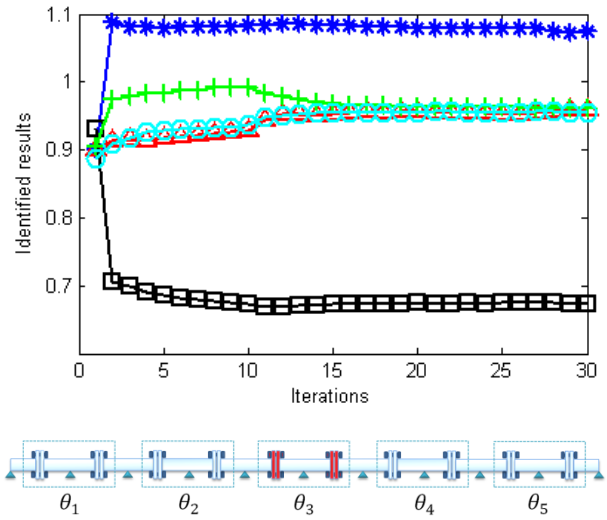

(c) Model class $\mathcal{C}_6$

Fig. 13. History of iterative simultaneous estimation by the particle filter-based approach for Case 5 in the numerical study.

(a) Periodically supported bolt-connected beam in laboratory

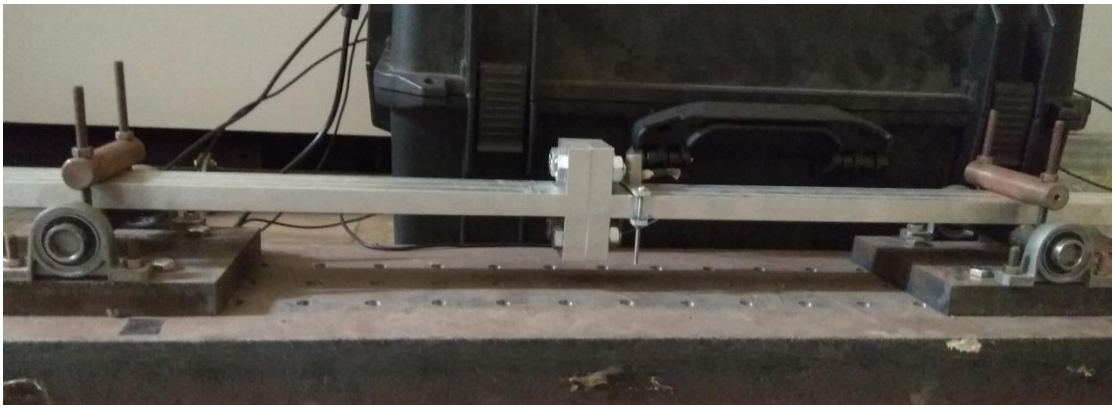

(b) One span of the periodically supported beam model

Fig.14. Laboratory model of a five-span periodically supported beam with bolted flange joints.

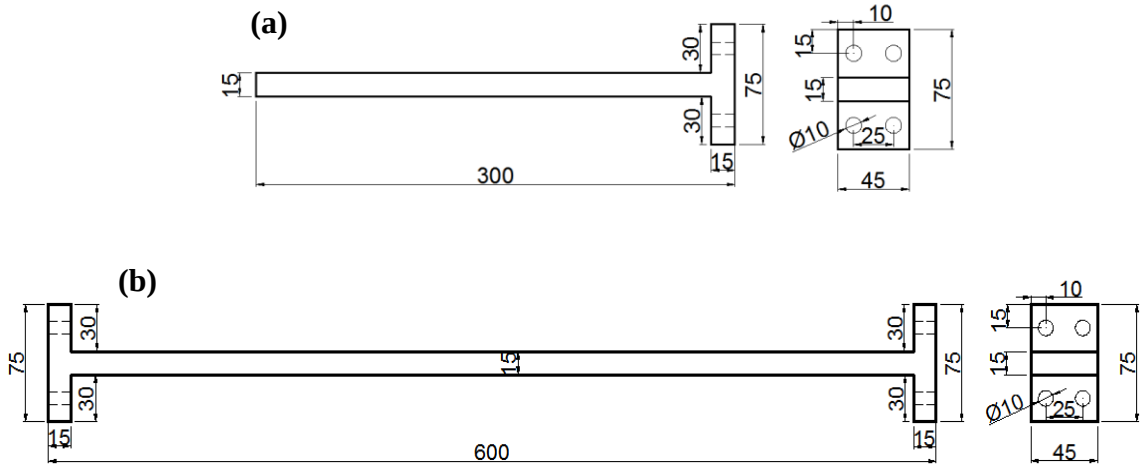

Fig. 15. Dimensions of the beam segments with bolted flange joints (units: mm): (a) beam segment of type I, (b) beam segment of type II.

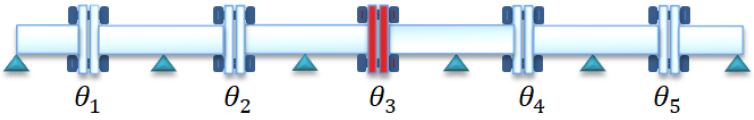

(a) Damage configuration in Case 2

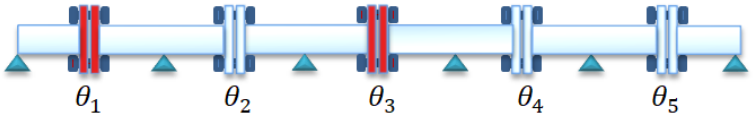

(b) Damage configuration in Case 3

Fig. 16. Damage configuration for the periodically supported beam model in experimental study (damaged bolted joints are marked in red)

(a) Experimental configuration

(b) Impact hammer

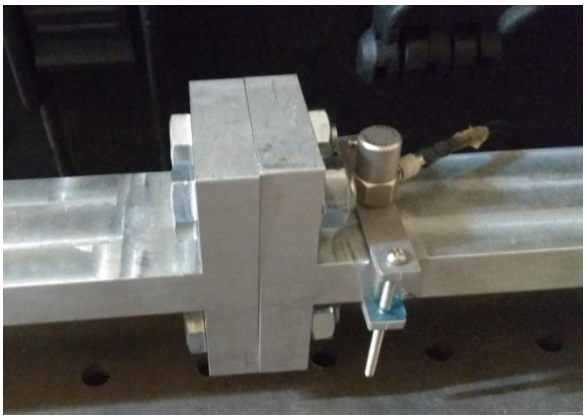

(c) Accelerometer with the fixture tool

(d) Signal acquisition box

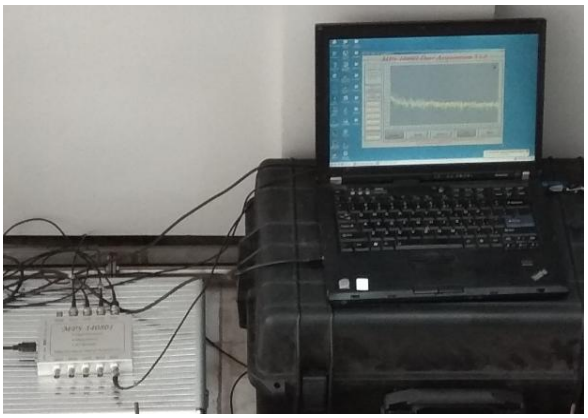

(e) Data acquisition system

Fig.17. Main experimental equipments for the laboratory periodic beam model.

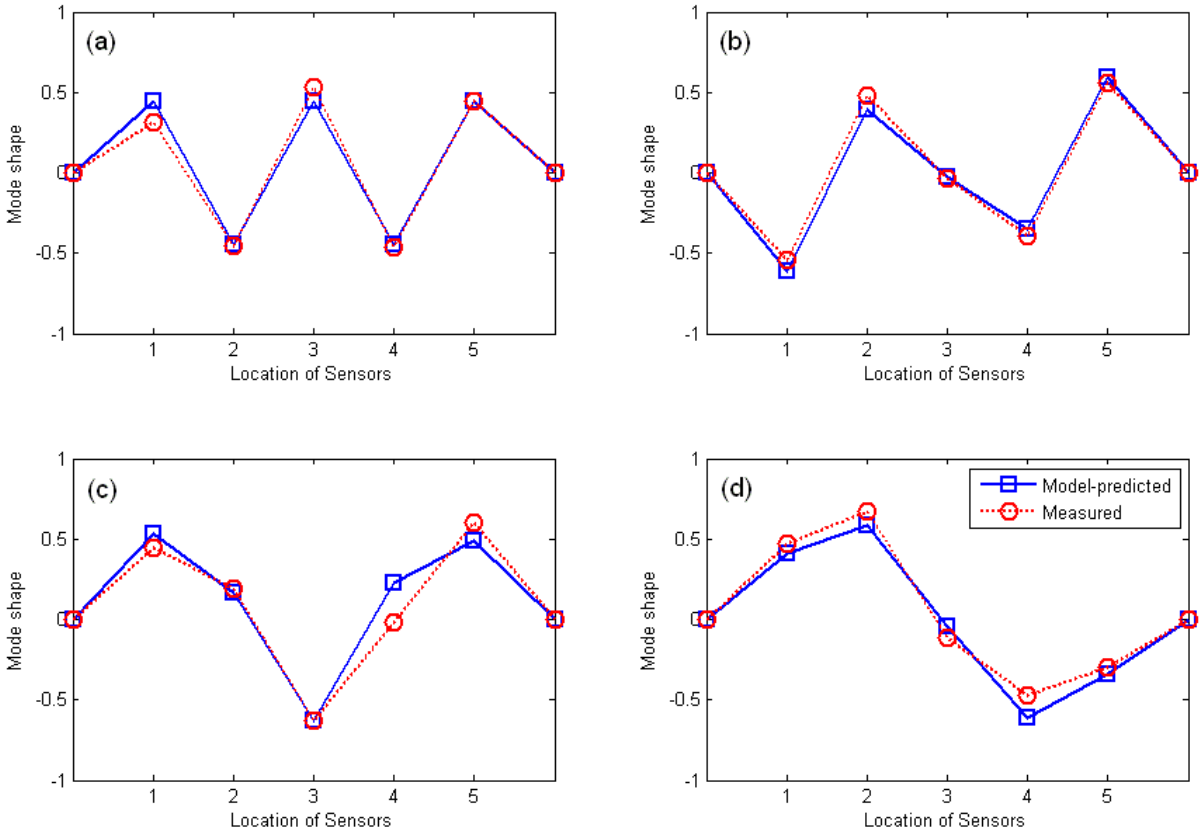

Fig. 18. Comparison of model-predicted and measured normalized mode shapes in the intact status: (a) mode 1 (MAC value: 0.975); (b) mode 2 (MAC value: 0.986); (c) mode 3 (MAC value: 0.919); (d) mode 4 (MAC value: 0.961)

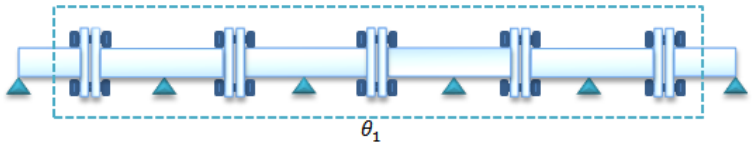

(a) Model class $\mathcal{C}_1$

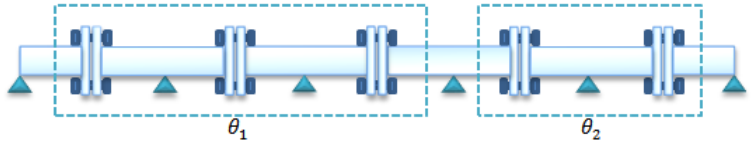

(b) Model class $\mathcal{C}_2$

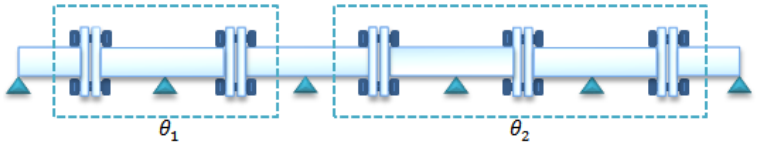

(c) Model class $\mathcal{C}_3$

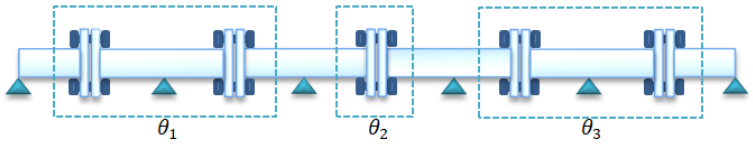

(d) Model class $\mathcal{C}_4$

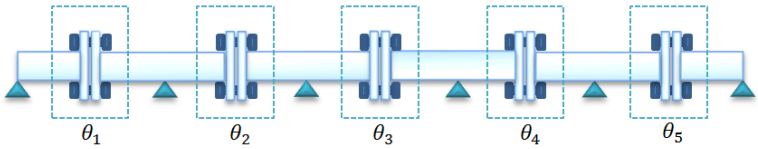

(e) Model class $\mathcal{C}_5$

Fig. 19. Different model classes for bolt-connected beam in the experimental study.

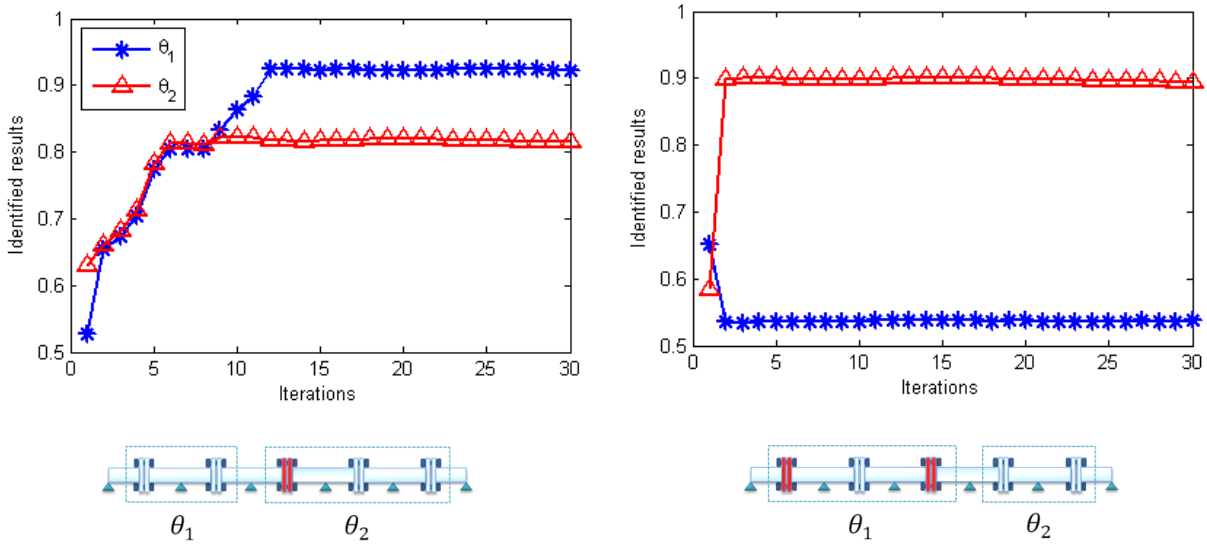

(a) Model class $\mathcal{C}_3$ in Case 2

(b) Model class $\mathcal{C}_2$ in Case 3

Fig. 20. History of iterative simultaneous estimation by the particle filter-based approach for the most plausible model classes of two damage cases in the experimental study.

Table 1

Geometric and material properties of periodic structure in the numerical study.

Parameters	**Values**
Young's modulus (E)	6.89×10^{10} N/m^2
Young's modulus of thin-layer element (E_{TL})	$0.001E$
Mass density (ρ)	2730 kg/m^3
Poisson ratio (μ)	0.3
Total number of spans/cells (N_P)	10
Length of each span (L)	0.6 m
Total length of periodic beam ($N_P L$)	6 m
Width of beam (W_B)	0.045 m
Height of beam (H_B)	0.015 m
Thickness of flange (T_F)	0.015 m
Height of flange (H_F)	0.075 m
Thickness of the thin-layer element (T_L)	0.005 m
Height of the thin-layer element (H_L)	0.01 m

Table 2

Numerical simulation cases for the ten-span periodic beam.

	Case descriptions
Case 1	$\theta_i = 1$ $(i = 1,2,\dots,10)$
Case 2	$\theta_2 = 0.7,\quad \theta_i = 1$ $(i = 1,3,4,\dots,10)$
Case 3	$\theta_5 = 0.7,\quad \theta_i = 1$ $(i = 1,2,\dots,4,6,\dots,10)$
Case 4	$\theta_2 = \theta_9 = 0.7,\quad \theta_i = 1$ $(i = 1,3,4,\dots,8,10)$
Case 5	$\theta_5 = \theta_6 = 0.7,\quad \theta_i = 1$ $(i = 1,2,\dots,4,7,\dots,10)$

Table 3

Results of model class selection for each numerical case.

		$p(\mathcal{C}_j\|\mathcal{D})$	$ln[p(\mathcal{D}\|\mathcal{C}_j)]$	**Likelihood factors**	**Ockham factors**
Case 1	$\boldsymbol{\mathcal{C}_1}$	**95.35%**	**69.65**	**87.06**	**-17.41**
	$\mathcal{C}_2$	3.73%	66.41	86.08	-19.67
	$\mathcal{C}_3$	0.70%	64.74	87.79	-23.06
	$\mathcal{C}_4$	0.13%	63.06	87.45	-24.39
	$\mathcal{C}_5$	0.07%	62.46	87.68	-25.22
	$\mathcal{C}_6$	0.01%	59.90	87.51	-27.60
Case 2	$\mathcal{C}_1$	0.11%	27.18	37.62	-10.44
	$\mathcal{C}_2$	0.06%	24.26	44.54	-20.28
	$\mathcal{C}_3$	0.15%	27.45	52.17	-24.72
	$\boldsymbol{\mathcal{C}_4}$	**48.26%**	**33.25**	**63.64**	**-30.39**
	$\mathcal{C}_5$	6.93%	31.31	62.90	-31.59
	$\mathcal{C}_6$	44.55%	33.17	84.03	-50.86
Case 3	$\mathcal{C}_1$	1.55%	26.73	32.02	-5.30
	$\mathcal{C}_2$	0.00%	16.59	40.75	-24.16
	$\boldsymbol{\mathcal{C}_3}$	**77.11%**	**30.64**	**57.16**	**-26.52**
	$\mathcal{C}_4$	0.37%	25.30	51.91	-26.61
	$\mathcal{C}_5$	10.44%	28.64	54.54	-25.90
	$\mathcal{C}_6$	10.53%	28.65	65.21	-36.56
Case 4	$\mathcal{C}_1$	0.85%	20.96	29.45	-8.49
	$\mathcal{C}_2$	1.41%	21.47	33.96	-12.49
	$\mathcal{C}_3$	0.30%	19.92	36.57	-16.65
	$\boldsymbol{\mathcal{C}_4}$	**57.61%**	**25.18**	**42.81**	**-17.63**
	$\mathcal{C}_5$	21.41%	24.19	43.53	-19.34
	$\mathcal{C}_6$	18.43%	24.04	48.81	-24.77
Case 5	$\mathcal{C}_1$	0.28%	21.93	30.60	-8.66
	$\mathcal{C}_2$	0.62%	22.72	32.72	-10.00
	$\boldsymbol{\mathcal{C}_3}$	**61.80%**	**27.32**	**57.48**	**-30.15**
	$\mathcal{C}_4$	0.63%	22.73	49.99	-27.25
	$\mathcal{C}_5$	13.25%	25.78	53.78	-28.00
	$\mathcal{C}_6$	23.43%	26.35	60.73	-34.38

Table 4

Identified results by particle filter method in the numerical study.

			$\boldsymbol{\theta_1}$	$\boldsymbol{\theta_2}$	$\boldsymbol{\theta_3}$	$\boldsymbol{\theta_4}$	$\boldsymbol{\theta_5}$
Case 2	$\mathcal{C}_1$	MEAN	**0.978**				
		STD	2.4E-3				
	$\mathcal{C}_2$	MEAN	**0.923**	0.986			
		STD	4.1E-3	4.5E-3			
	$\mathcal{C}_3$	MEAN	**0.837**	0.934	0.896		
		STD	2.4 E-3	7.1E-3	3.6E-3		
	$\boldsymbol{\mathcal{C}_4}$	MEAN	**0.893**	1.034	1.018		
		STD	3.4E-3	3.7E-3	3.5E-3		
	$\mathcal{C}_5$	MEAN	**0.778**	0.979	0.856	0.908	
		STD	2.9E-3	5.9E-3	3.8E-3	3.4E-3	
	$\mathcal{C}_6$	MEAN	**0.767**	1.063	1.027	0.926	1.047
		STD	8.6E-3	8.4E-3	7.4E-3	5.2E-3	4.7E-3
Case 5	$\mathcal{C}_1$	MEAN	**0.975**				
		STD	3.6E-3				
	$\mathcal{C}_2$	MEAN	**0.937**	**0.943**			
		STD	3.5E-3	3.1E-3			
	$\boldsymbol{\mathcal{C}_3}$	MEAN	1.000	**0.704**	0.998		
		STD	3.0E-3	4.0E-3	4.1E-3		
	$\mathcal{C}_4$	MEAN	1.016	**0.786**	0.991		
		STD	5.1E-3	5.4E-3	5.9E-3		
	$\mathcal{C}_5$	MEAN	1.080	**0.851**	**0.842**	1.041	
		STD	4.9E-3	5.2E-3	5.1E-3	4.4E-3	
	$\mathcal{C}_6$	MEAN	0.960	0.929	**0.711**	0.931	0.939
		STD	1.3E-2	8.3E-3	6.4E-3	5.7E-3	5.2E-3

Table 5

Model-predicted and measured natural frequencies (Hz).

Mode	Model predicted	Experiment				
		Healthy status		Damaged status		
		Case 1	Case 2	Changes	Case 3	Changes
1	80.55	80.53	77.64	-3.59%	76.59	-4.89%
2	89.74	90.52	89.79	-0.81%	88.31	-2.44%
3	112.41	102.09	99.73	-2.31%	98.44	-3.58%
4	141.15	134.05	132.81	-0.93%	129.32	-3.53%

Table 6

Results of model class selection for each experimental case.

		$p(\mathcal{C}_j\|\mathcal{D})$	$ln[p(\mathcal{D}\|\mathcal{C}_j)]$	**Likelihood factors**	**Ockham factors**
Case 1	$\boldsymbol{\mathcal{C}_1}$	**99.87%**	**-2.54**	**2.47**	**-5.01**
	$\mathcal{C}_2$	0.09%	-9.56	2.45	-12.01
	$\mathcal{C}_3$	0.04%	-10.32	2.41	-12.74
	$\mathcal{C}_4$	0.00%	-16.27	2.41	-18.68
	$\mathcal{C}_5$	0.00%	-20.97	2.45	-23.42
Case 2	$\mathcal{C}_1$	26.33%	-10.30	-3.22	-7.08
	$\mathcal{C}_2$	33.14%	-10.07	-2.76	-7.31
	$\boldsymbol{\mathcal{C}_3}$	**34.84%**	**-10.02**	**-2.73**	**-7.29**
	$\mathcal{C}_4$	4.40%	-12.09	-1.32	-10.77
	$\mathcal{C}_5$	1.29%	-13.32	-1.18	-12.14
Case 3	$\mathcal{C}_1$	19.88%	-11.24	-3.87	-7.37
	$\boldsymbol{\mathcal{C}_2}$	**21.18%**	**-11.18**	**-2.87**	**-8.31**
	$\mathcal{C}_3$	18.45%	-11.32	-2.88	-8.43
	$\mathcal{C}_4$	19.66%	-11.26	-2.67	-8.59
	$\mathcal{C}_5$	20.83%	-11.20	-2.55	-8.65

Table 7

Posterior mean and standard deviation of scaling parameters in the experimental study.

			$\boldsymbol{\theta_1}$	$\boldsymbol{\theta_2}$	$\boldsymbol{\theta_3}$	$\boldsymbol{\theta_4}$	θ_5
Case 2	$\mathcal{C}_1$	MEAN	**0.832**				
		STD	3.3E-2				
	$\mathcal{C}_2$	MEAN	**0.843**	0.941			
		STD	6.2E-2	7.1E-2			
	$\boldsymbol{\mathcal{C}_3}$	MEAN	0.923	**0.815**			
		STD	2.8E-2	3.7E-2			
	$\mathcal{C}_4$	MEAN	0.765	**0.210**	0.903		
		STD	3.5E-2	3.4E-2	4.5E-2		
	$\mathcal{C}_5$	MEAN	0.947	0.897	**0.205**	0.882	0.928
		STD	3.5E-2	4.2E-2	2.9E-2	3.6E-2	2.5E-2
Case 3	$\mathcal{C}_1$	MEAN	**0.743**				
		STD	2.4E-2				
	$\boldsymbol{\mathcal{C}_2}$	MEAN	**0.518**	0.895			
		STD	1.8E-2	2.2E-2			
	$\mathcal{C}_3$	MEAN	**0.527**	**0.753**			
		STD	6.5E-2	4.2E-2			
	$\mathcal{C}_4$	MEAN	**0.478**	**0.239**	0.699		
		STD	2.6E-2	2.4E-2	2.4E-2		
	$\mathcal{C}_5$	MEAN	**0.224**	0.765	**0.216**	0.851	0.894
		STD	4.5E-2	3.2E-2	3.3E-2	2.7E-2	2.9E-2